

Nuclear excitation functions for medical isotope production:
Targeted radionuclide therapy via natIr(d,2n)^{193m}Pt

Hannah Lovise Okstad Ekeberg

June 2020

Contents

1 Abstract	5
2 Targeted radionuclide therapy	7
2.1 Particle interaction in tissue	9
2.2 Production of radionuclides	12
2.3 ^{193m}Pt as a potential therapeutic agent	13
3 General nuclear reaction theory	17
3.1 Radioactive decay law	17
3.2 Nuclear reactions and reaction cross sections	19
3.2.1 Constraints in nuclear reactions	21
3.2.2 Deuterons and stopping power	23
3.3 Nuclear reaction models	24
3.4 Detection and identification of radionuclides	24
3.4.1 Gamma-ray spectrum	25
4 Experimental setup	27
4.1 Lawrence Berkeley National Laboratory's 88" Cyclotron	27
4.2 Detector calibration	27
4.2.1 Energy and peakshape calibration	29
4.2.2 Efficiency calibration	30
4.3 The stacked target activation method	30
4.3.1 Characterization of the target foils	31
4.3.2 Irradiation	31
5 Analysis	41
5.1 Analyzing the gamma-ray spectra	41
5.1.1 Background subtraction	45
5.2 End of beam activities	45
5.3 Deuteron beam current and energy assignment	46
5.3.1 Variance minimization for the deuteron transport calculations	49
5.4 Cross sections	50
5.5 Estimation of the beam current	50
5.5.1 Variance minimization of the deuteron transport calculations	52
5.6 Cross section measurements	54
A Statistics	59
B Tables	61
B.1 Product nuclei, Q-values and gammarays	61
B.2 Production cross sections	68
B.2.1 $^{nat}\text{Ir}(d,x)$	68

CONTENTS

Chapter 1

Abstract

In this thesis work, a stack of ten natural irridium (99.9%) foils were irradiated with a 33 MeV incident deuteron beam at the Lawrence Berkeley National Laboratory's 88-Inch Cyclotron, yielding ten cross section measurements from ca. 5 to 30 MeV in the activated foils as the energy decreases as the deuterons traverses through the foils. The motivation behind this experiment was to measure the $^{nat}Ir(d,x)$ reactions which have lack of data..., with a special emphasis on finding the energy-window inwhich optimizes the production of the auger-emitting radionuclide ^{193m}Pt which can have potential in targeted radionuclide therapy. In addition, ten monitor foils of nickel, copper and iron were placed within each compartment of irridium, to measure the deuteron current in each compartment, via the well-characterized monitor reactions $^{nat}Ni(d,x)^{61}Cu$, $^{56,58}Co$, $^t ext{nat}Cu(d,x)^{62,63,65}Zn$ and $^{nat}Fe(d,x)^{56}Co$.

The cross sections were estimated using the analogy to the activation equation for thin targets, $A_0 = N_T \cdot \Phi(E_d)\sigma(E_d)(1 - e^{-\lambda t_{irr}})$, where the energy of the deuteron beam was weighted-averaged over each foil. Prior to radiation, the number of target nuclei of each foil was characterized measuring the length across each foil and the mass. The deuteron-induced activity in each foil as a function of time since end of beam was obtained using gamma-ray spectroscopy on pre-calibrated high purity germanium detectors. The measured activities were fitted to decay curves to find the activity at the end of beam. Along with the weighted averaged beam current estimated from the monitor reactions, the flux weighted cross sections were estimated. This work along with previous experimental data suggests an energywindow from ca. 11 to 15 MeV which maximises the production of ^{193m}Pt . The highest measured cross section in this work was 148.98 ± 5.54 mb at 13.51 MeV. For irridium, the independent measurements of $^{188,190m2,194m2}Ir$ and $^{188,189,191,193m}Pt$, and the cumulative cross sections $^{188,189,190,192,194}Ir$ are reported. From the monitor foils, the first observed measurements of cumulative cross sections of ^{61}Co from copper, cumulative cross sections of ^{48}V , ^{51}Cr , ^{53}Fe from iron, the cumualative cross sections of ^{59}Fe and the independent cross sections of $^{56,57,57}Co$ are also reported in this work, along with the other products produced. The results are compared to experimental data from the EXFOR database, along with the nuclear reaction modelling codes TALYS, TENDL, CoH, ALICE and **EMPIRE**, using the default parameters to aid improvements of the codes, **which did not match the experimental data very well in general, in particular in magnitude.**

Chapter 2

Targeted radionuclide therapy

All written in this chapter needs to be rewritten as a lot of the text is just copied from various citations.

Today, multiple options for treatment of cancerous tissue are available, such as chemotherapy, surgery, immunotherapy, external beam therapy, brachytherapy and targeted radionuclide therapy. The latter three are treatment types utilizing ionizing particles to induce damage to the DNA. In external beam therapy X-rays, high-energetic gamma-rays, or accelerated particles like protons and heavier ions are focused externally towards the tumor, and in brachytherapy an unsealed radioactive source (usually a wire or pellet containing for instance a β -emitter), is placed in proximity to tumor (handbook of nuclear chemistry, p. 2180). Targeted radionuclide therapy is an emerging alternative, which can deliver a cytotoxic level of dose to the site of disease (handbook of nuclear chemistry p. 2180). It offers a patient-specific treatment dependent on choice of radiopharmaceutical which targets a type of tumor or cell. A radiopharmaceutical consists of a radionuclide and a cell-targeting molecule called a tracer. Meanwhile brachytherapy and targeted radionuclide therapy are limited by the cancer location and the existence of metastasis, along with required knowledge of the tumor to maximise the dose over the tumor and minimizing the dose to healthy tissue (Handbook of nuclear chemistry, p. 2180), targeted radionuclide therapy utilizes radiopharmaceuticals which are typically injected intravenously and utilized the biochemical pathways in the body. thus with an appropriate tracer, targeted tissue with a high uptake of the radiopharmaceutical will receive a high dose, and healthy tissue can be spared

A therapeutic agent need to have the two components optimized for the radiation from the radionuclide to have a high probability of being deposited in the tumor, and ideally cytotoxic dose to all cancerous cells within a tumor and sparing all healthy cells. The decay mode and radiation range are in coherence with the size and location, as well as the geometry of the tumor, and ranges from multicellular, cellular and subcellular ranges are typically accomplished with beta, alpha and auger electrons, respectively. However, geometrical factors of both the distribution and the tumor it self can have a degree of variations in the dose distribution due to differences in cross fire dose and the fraction of the radiation bound to the cell that is deposited in the tumor. Particularly apparent for micrometastatic disease which presents as small cluster of tumor cells, magnifying the impact of these factor. In addition, it is important to achieve a homogeneous dose deposition within the tumor, so that regrowth from an untreated subpopulation will be avoided. For the radionuclide, along with range and decay mode, the half-life production method, chemistry and biological behavior are important characteristics (all above in paragraph: handbook p. 2180-2182). For the tracer, a rapid blood clearance and transport (6, p. 145) and high uptake and retention in the tumor (9. p. 2) (special curriculum p. 4) are important characteristics. It can target the desired cells by for instance a specific receptor, enzyme, membrane, transporters or antigens (6, p. 145). Radiometals are also used, which consists of a bifunctional chelator, which is a molecule containing molecules which can donate a lone pair of electrons, like nitrogen, oxygen or sulfur. If the radiometal has an oxidation state of 3^+ , it will be tightly bound by the chelator, and can transported to the tumor (special curriculum p. 4-5).

Figure 2.1 shows an illustration of how a radionuclide is attached to a chelator, and is transported

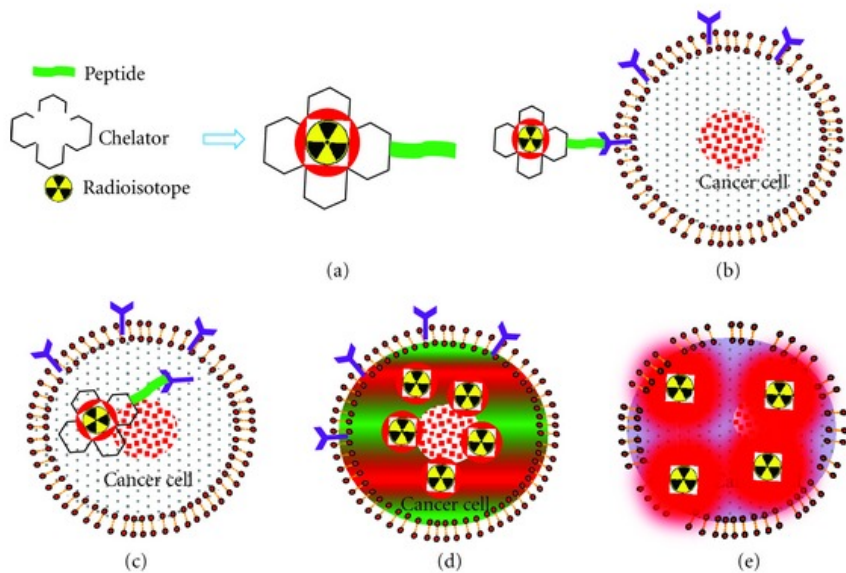


Figure 2.1: A radionuclide is bound to a chelating agent, and with a peptide, the radiopharmaceutical targets the cancer cells. Figure is from citation [8] in the special curriculum.

to cancer cells with a specific peptide.

Whenever something is cited like (3), it means citation 3 in special curriculum Special curriculum p. 4: as mentioned above there are many requirements before a radiopharmaceutical can be used clinically, there are physical properties concerning the radionuclide, such as physical half-life, decay-mode and decay product, radiation energy and in-tissue range, and biological properties concerning the tracer such as tissue targeting, biological half-life, retention in tumor and the uptake in healthy tissue (3). Thus, the radiopharmaceutical requires two components in which complement each other to deposit the dose in the cancerous tissue.

In nuclear medicine, the effective half-life of the radiopharmaceutical is important as it takes both the physical half-life and the time it takes for the radiopharmaceutical to be cleared or excreted from the body (3). Thus it should be long enough to permit radiosynthesis and quality control (handbook, chapter targeted radionuclide therapy). Should be compatible with the pharmacokinetics of localization in tumor and clearance from normal tissue. However, as for therapy, high radiation dose is desired, which is easier to achieve with shorter half life, so that should also be compensated for. The choice of radionuclide should match the uptake rate and the retention, to avoid radioactive waste handling and dose to healthy tissue (3). Therapeutic radionuclides typically have half-lives in order of a few hours to several days (9, p. 1) (special curriculum p. 4).

Knowledge about the decay products are also important, if unstable, how it the dose distributed, and how long range, half life etc, and if unstable, is the daughter contributing to a cytotoxic effect, or taking part of the natural processes in the body.

In addition, the chemical-biological properties are important, as it must be chemically possible to attach radionuclide to the targeting molecule. Also, the bond must be stable in the body, over a time period which is stable as long as the physical half life. (handbook p. 2185)

Along with the ability to use radionuclides in therapy, radionuclides can also be used for diagnostic purposes with imaging, either with positron emitters (positron emission tomography) in which annihilates with atomic electrons close to the site of decay, and sends out two 511 keV photons, or emission of a strongly fed gamma-decay energy which is detected (single photon emission tomography). The combination of a diagnostic and a therapeutic agent with similar properties so that the biochemical uptake in the body is a new approach in which can give information of how the uptake is distributed

in the body, and can image the state of decease after therapies (The beginning and development of the theranostic approach in nuclear medicine.... 86/90Y). This is called theranostics..

2.1 Particle interaction in tissue

Ionizing radiation are particles with sufficient energy to cause ionizations along the particle track, thus separating an atom and one or more electrons. The free electron(s) can ionize further, and the positive ion can cause undesired reactions. DNA is a large molecule with two strands bound in a double helix structure. Each strand is composed of sugar and phosphate groups, and nitrogenous bases which bind the two strands (biobook p. 11). These bases are called adenine & guanine and cytosine & thymine (always bound pairwise), and are bound through weak hydrogen bonds which are exposed for strand breaks. The cell is equipped with an impressive repair mechanism, and unless both strands of the DNA is damaged, called a double stranded break (DSB), most damages are repaired. Radiation damages in the DNA can be caused directly by the ionizing particle or indirectly via free radicals, which are subject to other ionizations. Since the body contains large amounts of water, ionization of water molecules giving for instance H^\bullet or OH^\bullet are important damaging factors. Damages induced in the DNA can be lethal to the cell and either cause apoptosis or mutation in which can cause cancer. In therapy, the goal is to make malignant cells to undergo apoptosis, thus DNA is referred to as the target (book, p. 9). Choosing a particle with a high probability of inducing damage will induce multiple double stranded breaks if passing near by (special curriculum).

Linear energy transfer (LET) describes the energy absorbed by the medium, and is defined as the average energy (typically in keV) deposited per unit length (typically measured in μm) of the density material (biobook, p. 101)

$$\text{LET} = \frac{dE}{dx} \quad (2.1)$$

To maximise the chances of inducing damages in the DNA and minimizing exposure of healthy tissue, choosing a particle with a high linear energy transfer is important in targeted radionuclide therapy. Figure 2.1 illustrates how β^- -particles, alpha-particles and auger electrons deposit energy on the scale of DNA.

Beta decays occur whenever there is an overweight in number of protons/neutrons. β^- : $n \rightarrow p + e^- + \bar{\nu}_e$. The contrary β^+ decay: $p \rightarrow n + e^+ + \nu_e$. Neutron mass is higher than proton mass with $2m_e \text{ MeV}/c^2$, thus energy threshold for beta+ reaction must overcome this. If not high enough E, electron capture happens: $p + e_{\text{atomic}}^- \rightarrow n + \nu_e$. For beta is distributed between three particles thus the energy is not discrete. Alpha decay occur when the nucleus is so large about to overcome Coulomb barrier. Thus emission of an alpha particle lowers the binding energy as the alpha particle carries a high B.E. These are discrete. Auger electrons are result from electron capture or internal conversion, which happens when a gamma-ray interacts electromagnetically with atomic electron, and emit with high energy. The vacancy in the atomic shell can lead to a cascade of X-rays and auger electrons with energies in the X-ray range. These energies are discrete, as the X-ray energy is discrete (minus atomic binding energy). From beta and sometimes alpha decay, the daughter nucleus is left in an excited state and decays by gamma-emission (all from special curriculum).

A medium consists of positively charged nuclei and negatively charged electrons. Charged particles have a short range in a medium compared to neutral particles, as the Coulomb force forces the particle to interact continuously along the path either by scattering inelastic with the atomic electrons or scattering elastic with the nuclei. Elastic scattering is the less dominant process, where the energy loss is small, as long as the nuclei in the medium are larger than the incoming particle(Techniques for Nuclear and Particle Physics Experiments, William R. Leo, p. 21). **Inelastic collisions dominates where the atomic electrons are either excited or ionized (which citation???? Instrumentation book?).** Under the assumption that the collision is elastic, the collision is head-on and the particle has high energy, the maximum energy transfer can be calculated using conservation of momentum and energy

$$Q_{\max} = \frac{4m_e M}{m + M} E \quad (2.2)$$

where m_e is the mass of an atomic electron, M is the mass of the incoming charged particle and E is the kinetic energy of the incoming charged particle¹. While LET describes the energy transferred per unit length, the stopping power describes the energy loss of a charged particle per unit distance. The collision loss for heavy charged particles (protons and above) at high energies is therefore low. The stopping power for heavy charged particles (protons and up) is described by Bethe-Block. As the particle slows down, the more energy per unit length will be deposited, as the charged particle picks up electrons. This is known as the Bragg peak. most of the energy is deposited near the end stop. The stopping power of heavy charged particles are proportional to the charge of particle and the inverse velocity squared. Therefore, particles with a higher charge will have a higher Bragg-peak and a shorter range in tissue, if energy was the same. This behaviour of heavy charged particles is especially useful in external beam therapy and is utilized to have a very specific dose over tumor as the dose before is low and the dose after bragg peak is zero (instrumentation, p. 27-28).

Electrons can experience energy loss either from collisions, or via the electromagnetic radiation that arises when electrons are losing energy (bremsstrahlung), due to the small mass. However, for energies up to a few MeV, the collision energy loss dominates (Techniques for Nuclear and Particle Physics Experiments, WilliamR. Leo, p. 37). For electrons, the maximum energy transfer per collision is half of the initial energy, which means that electrons lose energy fast via collisions. Electrons scatters rapidly, and changes direction continuously due to the equal mass of the atomic electrons. The energy loss of electrons fluctuates much more than heavy charged particles which is due to much greater energy transfer per collision and to the emission of bremsstrahlung. To absorb major part of the electron's energy, is a few collisions, and results in greater range straggling. (instrumentation p. 42)

Beta-electrons have a continuous spectrum of energies and absorption of beta decay electrons exhibit behaviour which is well approximated to an exponential form (instrumentation p. 42). Low energetic electrons are small in mass to large angle deflection by scattering from nuclei (p. 48).

Photons and neutrons however are neutral particles and are not energy-degraded. Instead neutral particles are attenuated as a function of distance traversed x and the absorption coefficient μ of the material

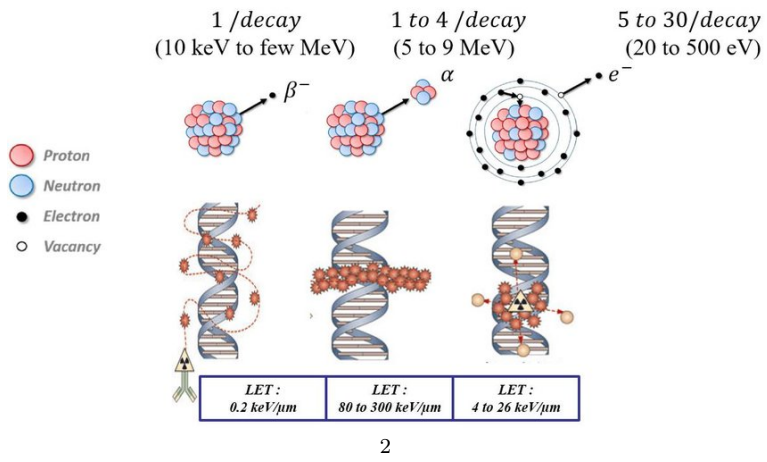
$$I = I_0 e^{-\mu x} \quad (2.3)$$

where I is the intensity as a function of distance and I_0 is the intensity at $x=0$ (

Figure 2.3 illustrates how various particles interact in a medium. For photons, there is an exponential tail, and for high energetic X-rays it is clear that there is a build up effect. For protons, the Bragg peak is very evident. For 22 MeV electrons, it is clear that there is bremsstrahlung energy loss due to the exponential tail.

Figure 2.4 shows an overview of the ranges of auger electrons, 5.3 MeV alpha particles, low and high energetic β^- particles of 0.15 MeV and 1.7 MeV. Thus β^- -particles have a relatively long range in tissue, and can be up to a few mm dependent on the energy spectrum (handbook, chapter TRNT (TARGETED RADIONUCLIDE THERAPY). Beta-particles have relatively low LET and are thus suited for treating large tumors, but the dose to healthy tissue is hard to avoid. Alpha-particles have short range in tissue, typically a one to a few cells in diameter. Has a high LET-value, radiation with $LET=100 \text{ keV}/\mu\text{m}$ has the distance between ionizing events is nearly identical to that between DNA strands increasing the probability of creating highly cytotoxic double strand breaks (handbook, TRNT). One of the major problems with alpha-emitters however is the decay products, as a typical alpha decay chain results in multiple emission of alpha and beta (??). For low energetic electron

¹<https://ocw.mit.edu/courses/nuclear-engineering/22-55j-principles-of-radiation-interactions-fall-2004/lecture-notes/energydeposhcp.pdf>



3

Figure 2.2: The figure illustrates how β^- -particles, α -particles and auger electrons deposit their energy on the scale of DNA.

4

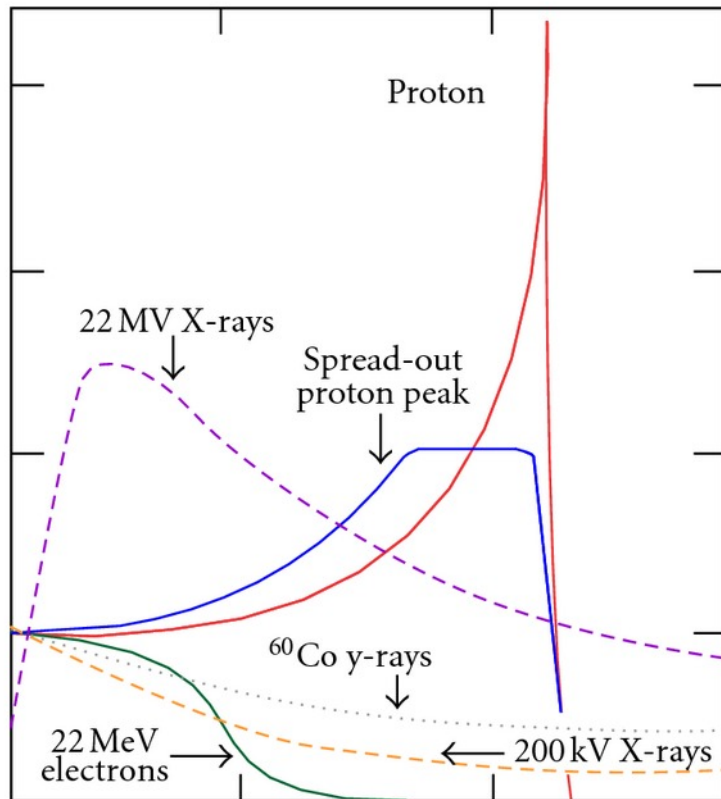


Figure 2.3: Medium depth along x-axis, energy deposition in tissue (or dose?) on y-axis. Find citation in special curriculum.

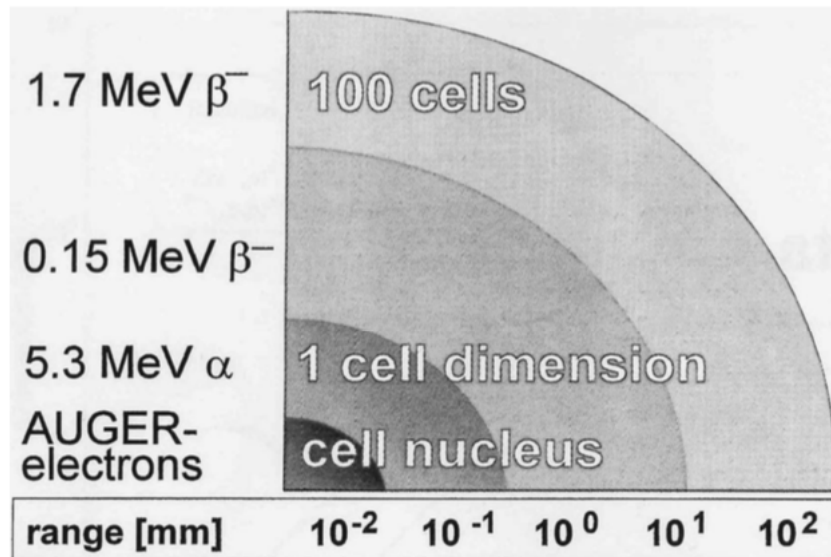


Figure 2.4: The figure illustrates the ranges of auger electrons, 5.3 MeV alpha particles and low and high energetic β^- particles.

emitters such as auger emitters, the range is so low that in order to deposit energy in the DNA, must be incorporated into the cellular nucleus. Thus, it will only affect the cell targeted, and as we can see in figure 2.1 when incorporated into DNA, will induce many breaks and kill cell!! (book: chapter targeted radionuclide therapy, whole paragraph)

2.2 Production of radionuclides

The radionuclide availability is an important factor, and must obviously be high. Reactors, cyclotrons and natural decay chains have traditionally been used as radionuclide sources (Handbook of ... , p. 2185). Proton rich nuclei are typically produced in accelerators/cyclotrons using positively charged particles, and neutron rich nuclei are typically been products of fission or produced in the neutron flux resulting from fission in a reactor. Thus therapeutic radionuclides producing β^- -emitters needs neutrons, which are the main source of reactors. With research reactors today aging ([3], in special curriculum p. 10), alternative production routes to produce critical medical radionuclides.

There are many different production routes available for a single radionuclide, dependent on choice of target, particle beam and beam energy. The production route has an associated reaction cross section which is dependent on the beam energy. The nuclear cross section data is very important in optimization of production processes, achieving the maximum yield of the desired radionuclide combined with the minimum level of radionuclidic impurities ([9], in special curriculum p. 3). A high degree of radionuclidic purity is required for therapeutical radiopharmaceuticals depending on the nature of the molecule that will be labelled, specific activity (GBq/mmol) may also be important consideration. It is impossible to chemically separate isotopes of the same element ([4], in special curriculum p. 10). We want to be sure that the what is injected into the patient does not have isotopic impurities which gives undesired dose to the tissue, nor will we have isotopes with no therapeutic effect, both for most effective treatment, but especially in cases where the body does not excrete the element from the body, and we can have poisoning. Carrier-free production which are molecules which exclusively contain the desired radionuclides is desired because it gives the highest specific activity. The only option to minimize impurities is to choose an appropriate energy window which minimizes the production of co-products.

There already exists large amounts of information on neutron induced reactions. However the information on charged particle induced reactions is not as strong so we need more data on this

behalf ([4] in special curriculum p. 10). Production of medical radionuclides should be cheap and available for everyday medical purposes. Cyclotrons good: Accelerators can be small in size and handled easily by medical personnel. Many hospitals which performs nuclear medicine even have a cyclotron facility on site, which is advantageous as its practical to avoid travelling logistics and to have medical radionuclide supply in proximity of examination/treatment site.

2.3 $^{193}\text{m}\text{Pt}$ as a potential therapautic agent

$^{193}\text{m}\text{Pt}$ ($t_{1/2}=4.33$ days) is an auger-emitting isomer which decays by isomeric transition (100%) to the long-lived $^{193}\text{g}\text{Pt}$ groundstate ($t_{1/2}=50$ years)

By replacing either of the stable nitrogen atoms with the PET-radionuclide ^{13}N ($t_{1/2}=9.965$ minutes), or by a radionuclide platinum, where ^{191}Pt ($t_{1/2}=2.83$ days, decay by electron capture (100%) to ^{191}Ir (stable)) , $^{193}\text{m}\text{Pt}$ and $^{195}\text{m}\text{Pt}$ ($t_{1/2}=4.010$ days, decay by isomer transition (100%) to $^{195}\text{g}\text{Pt}$ (stable)) is of special interest, cisplatin can be used for imaging or therapy⁵, but therapy is most common.

As ^{191}Pt is electron-capture emitter, can be used in imaging, with for instance 129.4 keV (38.0%) or 172.19 keV (43.2%). Combining ^{191}Pt with a therapautic agent might be possible for theranostic pair with either $^{193}\text{m}\text{Pt}$ or $^{195}\text{m}\text{Pt}$? Can be combined with therapy as it releases auger electrons?

Gamma-decay is a result of de-exitation of a nucleus with the release of a photon equal to the energy difference between the two states. The typical half-life of a populated excited state is less than 10^{-9} seconds, and states with longer half-lives are called isomeric states (Krane p. 175). This isomer decays by isomeric transition. In all decays, there are certain quantities which needs to be conserved; angular momentum, partiyl. Krane says that a multipole of order ℓ transfers angular momentum $\ell\hbar$ per photon (Krane p.333). A nuclear state has a definite angular momentum ℓ (ang mom + spin?) and parity, and if a gamma transition is to happen between two states the photon must connect the two states by conserving angular momentum and parity. In order for the quantity ℓ to be conserved, the angular momentum can be integers between

$$|I_i - I_f| \leq \ell \neq I_i + I_f \quad (2.4)$$

where i is initial and f is final. I is the total spin (angular momentum and spin). The parity decides wether the radiation is electric multipole or magnetic multipole (equations from Krane p.311)

$$\pi(ML) = (-1)^{\ell+1}, \quad \pi(EL) = (-1)^\ell \quad (2.5)$$

There are three populated states, the isomer state at 149.8 keV, with nuclear spin $13/2^+$ (4.33 d), a state at 14.3 keV with nuclear spin $5/2^-$ (2.52 ns), a state at 1.6 keV with nuclear spin $3/2^-$ (9.7 ns) and the ground state at 0.0 keV with nuclear spin $1/2^-$ (50 y)<https://www.nndc.bnl.gov/nudat2/getdecayscheme.js>

For the decay of $^{193}\text{m}\text{Pt}$ (E level=149.8 keV) to the excited state (E level=14.3 keV), the spin and parity changes from $13/2^+$ to $5/2^-$, which gives possible values for $\ell = 4, 5, 6, 7, 8, 9$. The electric decays have even parity when $\ell=\text{even}$, and magnetic has even when $\ell=\text{odd}$. If parity is unchanged in the decay ($\Delta\pi=\text{no}$), the electric multipoles are even and magnetic multipoles are odd. If the parity does change ($\Delta\pi=\text{yes}$) there would be odd electric and even magnetic multipoles. Hence for the possible transitions between $13/2^+$ to $5/2^-$ are whenever $\Delta\pi=\text{yes}$ and $\ell = 4, 5, 6, 7, 8, 9$, which gives possible M4, E5, M6, E7, M8 and E9 transitions.

In general, the lowest possible multipole dominates, and the emission of a multipole of one order higher ($\ell + 1$ than ℓ) is reduced by a factor ca. 10^{-5} (Krane, p. 335). Thus a multipole of order 4 or 5 has a low probability of occurring and thus the isomer has a long half-life. In comparison, the decay from $5/2^-$ to $3/2^-$ gives possible radiation $\ell = 1, 2, 3, 4$, $\Delta\pi=\text{no}$, gives possible M1, E2, M3, E4 and the same for decay from $3/2^-$ to $1/2^-$.

⁵https://www.sciencedirect.com/science/article/pii/S0969804399000822?casa_token=ZLJ8YPQzGZMAAAAAA:264QzKWpH8Kv6iHotiGMeoHTk8jKqmnoDgf709SrAD8BUWVwbRXriZbHgkYOtHg-2qyX3Hvt9E

Whenever gamma-decay is possible, another process called internal conversion is competing. It is an electromagnetic process where the nucleus electromagnetically with the atomic electrons, and an atomic electron is emitted instead of the photon (Krane, chapter 10, p. 341). The kinetic energy of the emitted electron is the transition energy minus the electron binding energy

$$T_e = \Delta E - B \quad (2.6)$$

where B is the binding energy. The emitted electron is called a conversion electron, and the energy is comparable to the gamma-ray energy. The conversion electron varies with the atomic orbital (Krane, p.??), and the electrons following internal conversion are in a spectrum of different discrete energies. The transition energy must be higher than the electron binding energy, and as a consequence the electron is labelled with the shell it was emitted from (remember that atomic shells are labelled with n: n=1=K, n=2=L, n=3=M, n=4=N, etc).

For ^{193m}Pt , internal conversion is highly favoured before gamma-decay, thus the observed gamma in gamma-ray spectroscopy is difficult. The total probability is the summed decay probability for gamma-decay and internal conversion

$$\lambda = \lambda_\gamma + \lambda_{\text{IC}} \quad (2.7)$$

and the internal conversion coefficient α can be defined as

$$\alpha = \frac{\lambda_{\text{IC}}}{\lambda_\gamma} \quad (2.8)$$

High values for α indicates high probability of internal conversion relative to the probability of gamma emission but the coefficient diverges towards infinity when λ_γ reaches towards zero, which for instance is when the gamma transition is zero. In general, the coefficient increases Z^3 , which will give a much greater coefficient for heavy nuclei than for lighter nuclei. In addition the coefficient decreases rapidly (ca. $E^{-2.5}$) with increasing transition energy. The multipole order also affects the coefficient, where a higher multipole order indicates a higher value. For higher atomic shells than the K shell ($n=1$) the coefficient decreases like n^{-3} (Krane chapter 10, p. 346).

From a therapeutic point of view, the most important process is the process which occurs after the release of the conversion electron. There is a vacancy in the shell following the emission of the atomic electron, and an electron from a higher shell or subshell fills this vacancy. Radiative or non-radiative processes can take place after to conserve energy ⁶. To conserve energy, an X-ray with the energy equal to the difference between the atomic states can be emitted, or that X-ray can interact electromagnetically with atomic electrons in same subshell, a higher subshell or shell (remember shell: n=1,2,.., subshell: spdf..). Dependent on where the ejected electron originated from, the electrons are called super Coster-Kronig, Coster-Kronig or auger electrons respectively. In practice the vacancy moves up to higher atomic shells and the result is a cascade of electrons and Auger electrons, until the reaction "fades out". Due to the low energies, they need to be located close to the cellular nucleus or incorporated into the DNA to induce damage (Handbook of nuclear chemistry, p. 2203). When incorporated into DNA they are equally almost effective as alphaemitters

Energy loss of low E auger electrons. In this energy region, is due to collision loss, not bremsstrahlung. Deflects frequently due to low mass, and the max energy loss is $T_e/2$ per collision, as described in equation 2.2.

General stuff ^{193m}Pt : Cellular nucleus is approximately $6\mu\text{m}$, while thickness of DNA is ca 2 nm (wikipedia). Range of the electrons from the decay is between 3.29nm - $231\mu\text{m}$, according to simulation done by Howell (1992)

Production: there are multiple ways that this isomer can be produced, either in a neutron field in a reactor, or in a charged particle accelerator like a cyclotron: $^{192}\text{Pt}(n,\gamma)$ or via $^{192}\text{Os}(\alpha,3n)$. One

⁶<https://sci-hub.tw/https://doi.org/10.1118/1.596927>

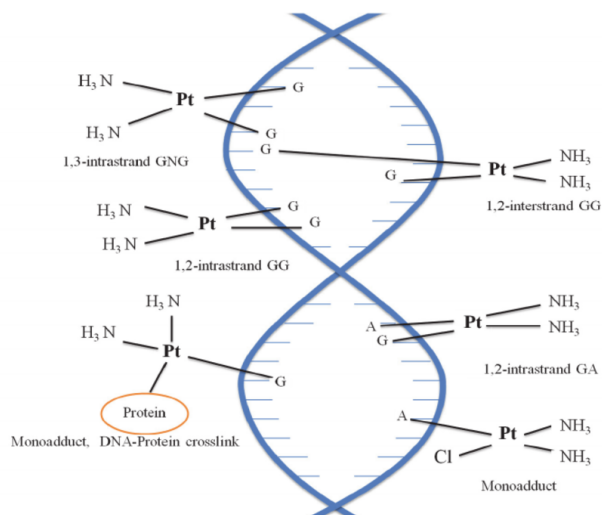


Figure 2.5: A DNA Repair Protein BRCA1 as a Potentially Molecular Target for the Anticancer Platinum Drug Cisplatin - Scientific Figure on ResearchGate. Available from: https://www.researchgate.net/figure/Common-cisplatin-DNA-adducts-and-functions-For-instance-the-platination-of-human-serum_fig2_21919257 [accessed 12 Apr, 2020].

of the issues with production is that ^{193}mPt (and ^{195}mPt) are difficult to produce with high specific activity

By itself, not useful for imaging. ^{191}Pt and ^{195}Pt can. Can replace stable N with ^{13}N , but the half life is so short that the radionuclide can not image the distribution it self, so not as a theranostics pair?? or does cisplatin distribute so fast within the body?

Pt-poisoning

Chapter 3

General nuclear reaction theory

paragraph based on special curriculum need to rewrite this part as some of this is already mentioned above.. Medical radionuclides can be produced directly using charge particle (cyclotron) or neutron beams (reactors), or indirectly using radionuclide generators or fission (reactor). Medical radionuclides are typically produced in reactors, cyclotrons or by a longer lived-parent decaying into a short-lived daughter in a radionuclide generator system. In general, the production should be cheap, available. Today many radionuclides are only produced in reactors, which is the main source of neutrons, and with reactors aging (Chai Hong Yeong, Mu hua Cheng, and Kwan Hoong Ng. Therapeutic radionuclides in nuclear medicine: Current and future prospects. Journal of Zhejiang University: Science B, 15(10):845–863, 2014.), we need alternative routes to produce critical radionuclides. Cyclotrons have many benefits, like size so that it can be produced directly at the site of usage. One of the major disadvantages is that there is a need to enriched targets to get the desired reaction, and those can be very expensive. Along with high beam intensity the melting of the target can give challenges, so target cooling techniqueis need to be there.

In order to create isotopes, nuclear reactions need to occur. There are many different production routes available for a single radionuclide, which is dependent on multiple factors such as choice of target, incident particle-beam and beam energy. To each reaction route, there is an corresponding excitation function which tells us how probable the reaction channel is at various energies. The nuclear reaction data is very important for the optimization of the product, achieving minimal level of isotopic impurities and maximum yield (S M Qaim, R Capote, and F Tarkanyi. Nuclear Data for the Production of Therapeutic Radionuclides. Trs 473, (473):395, 2011., p. 3).

Isotopic purity is important as it is impossible to separate isotopes of the same element

Using charged particles instead of neutrons allows for measurement at multiple energies as the particle energy degrades in the foils. The neutron energy is not degraded in the same way, due to electric neutrality, thus can only give cross section at one single energy.

3.1 Radioactive decay law

where to place this?

From here based on Krane chapter 6 ¹

The activity of a nucleus is defined as the number of decayed nuclei per unit time of a radioactive product, which is equal to the radioactive decay rate

$$A = \frac{dN}{dt} = -\lambda N \quad (3.1)$$

where N is the number of nuclei, t is the time and λ is the decay constant. Solving equation 3.1 gives number of decayed products at time t

$$N(t) = N_0 e^{-\lambda t} \quad (3.2)$$

¹<https://faculty.kfupm.edu.sa/phys/aanaqvi/Krane-Ch-6.pdf>

Since $N \propto A$, the relations $\frac{N_0}{A_0} = \frac{N(t)}{A(t)}$ are valid, and we can rewrite the equation 3.2 to

$$A(t) = A_0 e^{-\lambda t} \quad (3.3)$$

This accounts for single nucleus decaying into a daughter product, without anything first decaying into the parent nucleus. However it is common that a radioactive nucleus decays into another radioactive nucleus. Hence the daughter activity will increase due to feeding from the parent. For multiple decay, Bateman equation is used describing the activity in nucleus n of the decay chain (Voyles2018, which article??)

$$A_n = \lambda_n \sum_{i=1}^n \left[\left(A_{i,0} \prod_{j=i}^{n-1} \lambda_j \right) \cdot \left(\sum_{j=i}^n \frac{e^{-\lambda_j t}}{\prod_{i \neq j}^n (\lambda_i - \lambda_j)} \right) \right] \quad (3.4)$$

where A_n is the activity of nuclei n in the decay chain, with the corresponding decay constant λ_n . The equation sums over all nuclei in the decay chain. $A_{i,0}$ is the initial activity of nucleus i, and j is the nucleus which is feeding into nucleus i.

If a target of stable nuclei is assumed, which is exposed to a particle beam which induces various nuclear reactions, the constant rate of production of a specific reaction is dependent on the number of target nuclei, the current of flux of the particle beam and the reaction cross section

$$R = N_T \Phi \sigma \quad (3.5)$$

where R is the production rate, N_T is the number of target nuclei, Φ is the beam current or flux and σ is the reaction cross section. In the assumption of the production rate being a constant value, the number of transformed target nuclei is small in comparison to the total number during the irradiation time. The number of produced nuclei from a specific reaction per unit time is thus the produced nuclei minus the decayed nuclei (activity)

$$dN = R dt - \lambda N dt \quad (3.6)$$

which has the solution

$$N(t) = \frac{R}{\lambda} (1 - e^{-\lambda t}) \quad (3.7)$$

From equation 3.1, the total activity produced during irradiation time t is thus

$$A(t) = R(1 - e^{-\lambda t}) = N_T \Phi \sigma (1 - e^{-\lambda t}) \quad (3.8)$$

At the end of beam, the activity is denoted as A_0 , and t is the irradiation time:

$$A_0 = N_T \Phi \sigma (1 - e^{-\lambda \Delta t_{\text{irr}}}) \quad (3.9)$$

When a target is irradiated, the activity of the product nucleus will increase until secular equilibrium is achieved, which is when the product rate and decay rate are constant. Hence it is not necessary to irradiate a target for more than 2-3 half lives.

If a spectrum is counted at a delay time Δt_d after end of beam with a counting time Δt_c the total number of decayed products are

$$N_D = \int_{\Delta t_d}^{\Delta t_d + \Delta t_c} A(t) dt \quad (3.10)$$

Using equation 3.3 for $A(t)$, the solution to the above equation is

$$N_D = \frac{A_0}{\lambda} e^{-\lambda \Delta t_d} (1 - e^{-\lambda \Delta t_c}) \quad (3.11)$$

which again is equal to

$$N_D = \frac{A(t)}{\lambda} (1 - e^{-\lambda \Delta t_c}) \quad (3.12)$$

We can only know the number of decayed products which are detected. This is dependent on the efficiency of the detector, the intensity of the gamma-rays and the true number of decayed products

$$N_C = N_D \epsilon I_\gamma \quad (3.13)$$

where N_C is the number of observed/ counted gamma-rays, ϵ is the efficiency of the detector and I_γ is the gamma-ray intensity.

Thus, we can obtain an expression for $A(t)$ after a delay time:

$$A(t) = \frac{N_C \lambda}{\epsilon I_\gamma (1 - e^{-\lambda \Delta t_c})} \quad (3.14)$$

Again using 3.3 for $A(t)$, the above expression can be rewritten using A_0 and the delay time Δt_d

$$A_0 = \frac{N_C \lambda}{\epsilon I_\gamma (1 - e^{-\lambda \Delta t_c}) e^{-\lambda \Delta t_d}} \quad (3.15)$$

3.2 Nuclear reactions and reaction cross sections

talys 1.9 in reader can contain important info!

A nuclear reaction occurs when a collision between two nuclei or a nucleus and a subatomic particle takes place. Collision between an accelerated subatomic particle or small nucleus and target nuclei is common in isotope production. A nuclear reaction is denoted as

$$X(a, b)Y \quad (3.16)$$

where X is the target, a is the incoming projectile, b is the outgoing decay channel and Y is the product of the nuclear reaction (Krane, chapter 11.1). There are multiple processes which can occur, radiative capture is the process where a particle is captured and a γ -ray is emitted in a (x, γ) process. If the incoming and outgoing particle is the same, it is a scattering process, where elastic scattering leaves the target nucleus in the energy same state, and inelastic if the target nucleus is in an excited state. In these type of experiments however, we are interested in emission of particles to create products in which we can measure the reaction cross section.

In a nuclear reaction, the total energy and linear momentum, proton and neutron number, angular momentum and parity are conserved quantities (assuming no meson formation) (Krane, p.380). In the low energy-region in which isotope production typically takes place (180 MeV?), compound nucleus reactions take place, where an incoming particle and target nucleus merges by sharing the kinetic energy on all nucleons, and particle emission takes place to reduce the excess energy. ²Involves nucleon nucleon interactions, lead to a complete thermal equilibrium inside the CN. Releases energy by emission of neutrons, protons, alpha particles and gamma rays. A consequence of equilibrium is that the decay of CN should not depend on the way it was formed. "forgets" in all the collisions. Consequently, the decay of the compound nucleus depends only on the mass and atomic numbers, excitation energy and angular momentum. The contrary are direct reactions, where an incoming particle interacts (over such a short time period) so that the incoming particle only interacts with one single nucleon, typically on the surface of the target nucleus (thus probably in high nucleon shells, with high spin). Angular distributions of direct reaction products are sensitive to the momentum transfer and parity change during the reactions. Thus based on the selection rules from angular momentum and parity conversion the angular distribution measurements in direct reactions yield spin and parities of states populated in the exit channel. Write about feeding to the compound peak???. So in general;

²blue text:<https://web-docs.gsi.de/wolle/TELEKOLLEG/KERN/LECTURE/Fraser/L24.pdf>

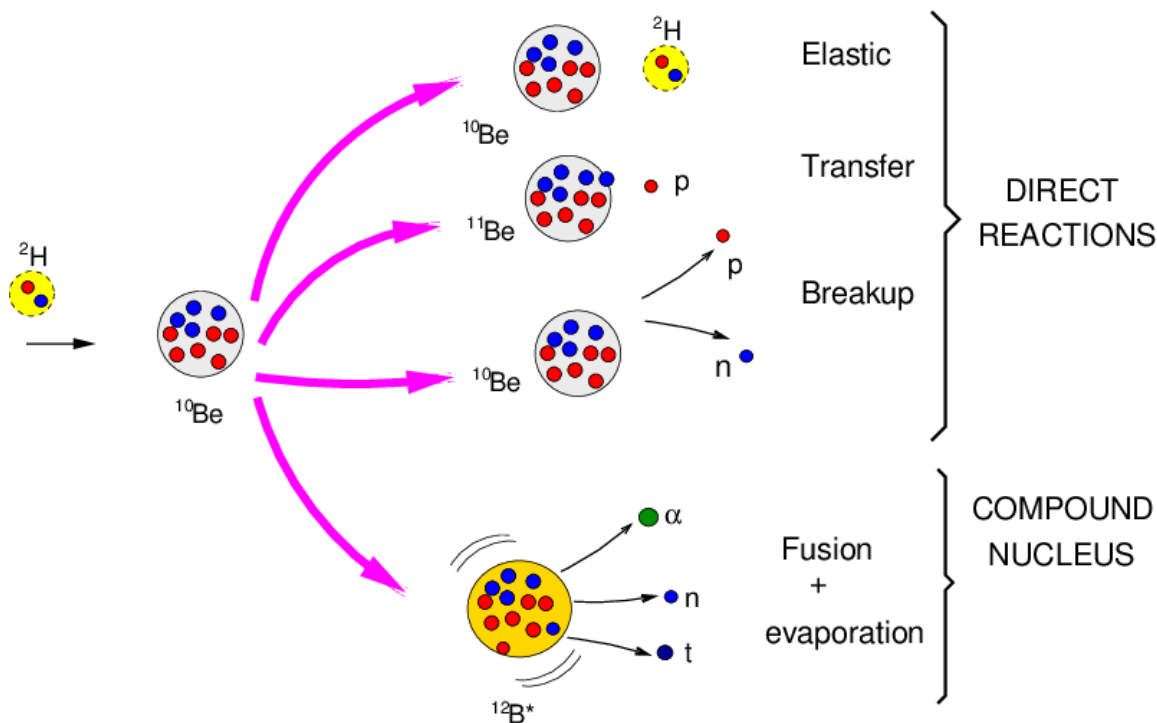


Figure 3.1: Models for nuclear reactions with weakly-bound systems - Scientific Figure on ResearchGate. Available from: https://www.researchgate.net/figure/Direct-and-compound-nucleus-reaction-channels-taking-place-in-a-d-10-Be-reaction/fig8_326366718 [accessed 13 May, 2020]

emission of protons and neutrons are more fed, because the probability of emitting one single nucleons is easier for the system. Since the reaction forgets the incoming projectile, and interacts with the whole nucleus, the prob of emission of t, ^3He and d is lower, and the binding energy does not do that the channel is more fed, its only a lower Energy threshold. For alpha particles however, the binding energy which is about 28 MeV lowers the energy quite a lot, therefor favourable if Coulomb barrier is low enough?

The cross section for a reaction can be divided into the cross section of the formation of the compound nucleus via interaction with the incoming projectile a, and the probability that the compound nucleus decay by decay channel b. The total reaction cross section is thus the sum of all the different reaction channels (Handbook of nuclear chemistry, p. 157 (nuclear reactions)),

$$\sigma = \sum_b \sigma(a, b) \quad (3.17)$$

where b can be multiple particles. The general equation which is used to calculate cross sections in this experiment (solving equation 3.15) is the following equation

$$\sigma(E) = \frac{A_0 \cdot t_{\text{irr}}}{N_T \cdot \Phi(E)(1 - e^{-\lambda t_{\text{irr}}})} \quad (3.18)$$

where A_0 is the end of beam activity of the resulting product nucleus (Y), t_{irr} is the irradiation time, N_T is the number of target nuclei (X), $\Phi(E)$ is the projectile flux or current (a), and λ is the decay constant of the product nucleus.

(
The compound nucleus model (Bohr, 1936) is a model which describes the formation of a compound nucleus by absorption of an incoming projectile by a nucleus close enough to interact with the strong nuclear force, and the decay of the compound nucleus. The kinetic energy shared between the incoming projectile and the nucleon which was struck leads to multiple collisions with other nucleons and rapid

exchange of energy. The energy is distributed throughout the nucleus, leaving the original nucleus in an highly excited state. The average energy per nucleon is not sufficient to overcome the binding energy of the nucleus, but due to the statistical distribution in energies there is a probability that one or more nucleons may get sufficient energy to escape the nuclear potential (Krane, chapter 11.10, p. 416). This is decay of the compound nucleus, and this will lower the excitation energy. We can include the formation of the compound nucleus in the nuclear reaction as



where C^* is the excited compound nucleus (Krane, chapter 11.10, p. 416)

For each possible decay channel of the compound nucleus, there is an associated probability or cross section, which is dependent on the energy of the incoming projectile. A function which evaluates the various cross sections at different energies is called an excitation function. In figure 3.2, the excitation function of the reactions channels for the platinum isotopes $^{188,189,191,193m}\text{Pt}$ resulting from deuterons on natural iridium is plotted (using TENDL nuclear reaction code [cite](#)). Natural iridium consists of two stable isotopes, ^{191}Ir (37.3% abundance) and ^{193}Ir (62.7% abundance). ^{193m}Pt can only be produced from ^{193}Ir , ejecting 2 neutrons in the process, which can be denoted as $^{193}\text{Ir}(\text{d},2\text{n})^{193m}\text{Pt}$ (^{193}Pt is the compound nucleus formation of deuteron on ^{191}Ir , which has a low production cross section). The other platinum isotopes can be produced as $^{191}\text{Ir}(\text{d},2\text{n})^{191}\text{Pt}$ or $^{193}\text{Ir}(\text{d},4\text{n})^{191}\text{Pt}$, $^{191}\text{Ir}(\text{d},4\text{n})^{189}\text{Pt}$ or $^{193}\text{Ir}(\text{d},6\text{n})^{189}\text{Pt}$ and $^{191}\text{Ir}(\text{d},5\text{n})^{188}\text{Pt}$ or $^{193}\text{Ir}(\text{d},7\text{n})^{188}\text{Pt}$. For each reaction route possible, there is a resulting compound peak, hence, ^{193m}Pt has only one peak, and the other platinum isotopes has two. The desired particle emission is energy dependent, and the higher energy provided to the compound nucleus, the probability that more particles will be emitted is higher (Krane, chapter 11.10, p. 419). When a specific isotope is desired, the excitation function can tell us which energy window that maximizes the production and most importantly minimizes particularly other isotopes of the same element, due to the difficulty of separating same chemical elements.

3.2.1 Constraints in nuclear reactions

The potential energy of a nucleus is the sum of the attractive well from the strong nuclear force and the repulsive Coulomb barrier which acts repulsive between charged particles and the nucleus, acting long range (p. 152, Handbook of nuclear chemistry). The radius of the potential well is up to a few femtometer. For a positively charged particle induced nuclear reaction, the energy of the particle should exceed the barrier, or there will be an elastic scatter. However, there is a chance of tunneling, which drops with a factor $1/r$ where r is the distance from the center of the nucleus (Handbook of Nuclear Chemistry, chapter 3 - Nuclear Reactions, section, 3.2.3). The barrier also constraints the emission of particles for a decay channel of the compound nucleus, as the energy for an outgoing decay channel of positive particles must exceed the barrier.

The height of the Coulomb barrier is dependent on the radius and charge of the incoming or outgoing particle a and the target nucleus b .

$$U_{\text{Coulomb}} = \frac{1}{4\pi\epsilon_0} \frac{e^2 Z_a Z_b}{r_a + r_b} \quad (3.20)$$

In addition, there is a centrifugal barrier, which can constraint some of the incoming particle energy in rotational energy, [which depends on the angular momentum of the incoming particle and and the nucleus???](#) (handbook of nuclear chemistry p. 155.)

$$U_{\text{centrifugal}} = \frac{\hbar\ell(\ell+1)}{r^2} \quad (3.21)$$

The sum of the barriers are the total barrier but the Coulomb barrier is the most important. In a nuclear reaction, the mass-energy is conserved, which is denoted as the Q-value. The reaction Q-value is the difference in masses between before and after the nuclear reaction occurred (Krane, chapter 11.2). It is defined as

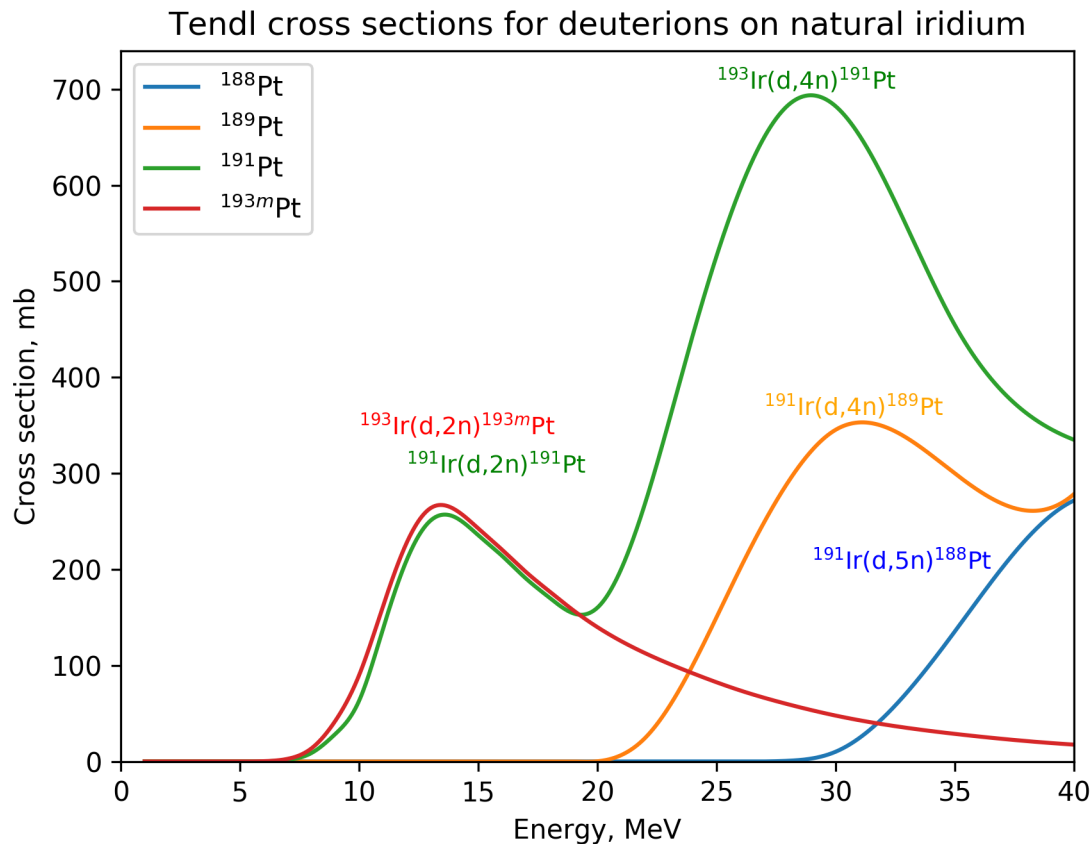


Figure 3.2: Reaction cross sections provided by Tendl for the reactions ${}^{\text{nat}}\text{Ir}(d,x)^{188,189,191,193m}\text{Pt}$

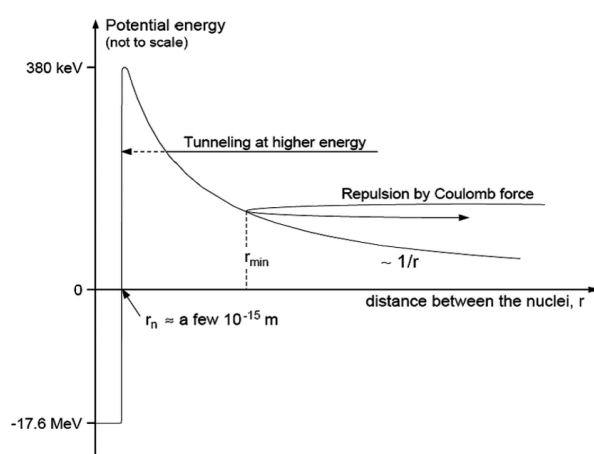


Figure 3.3

$$Q = (m_i - m_f)c^2 = (m_X + m_a - m_Y - m_b)c^2 \quad (3.22)$$

where m_i is the initial mass, m_f is the final mass and c is the speed of light. If $Q > 0$, then the reaction is exoergic, which means that energy is released in the reaction. There is no threshold energy of the projectile required for the reaction to occur, if only the projectile is present the reaction can occur. If $Q < 0$, then the reaction is endoergic, which means that the kinetic energy of the incoming projectile is converted into nuclear mass or binding energy. For endoergic reactions to occur, there is a minimum threshold energy of the projectile in order for the reaction to happen, which is defined as (Krane, 11.2, p. 382)

$$E_{\text{threshold}} = (-Q) \cdot \frac{m_Y + m_b}{m_Y + m_b - m_a} \quad (3.23)$$

The energy threshold thus depend on the Q-value, the Coulomb barrier for charged particles, and the centrifugal barrier if angular momentum $\ell \neq 0$. The parity though depend, even numbers of ℓ mix with even, and odd with odd (Handbook of Nuclear Chemistry, chapter 3Nuclear Reactions, section, 3.2.3). This gives an indication on when a reaction can energetically occur, but does not tell us how probable the reaction is.

The binding energy is the mass-difference between the nucleus as a whole, and the number of protons and neutrons added

$$B = c^2(z \cdot m_p + n \cdot m_n - m_N) \quad (3.24)$$

where z is the number of protons, n is the number of neutrons, m_p is the proton mass, m_n is the neutron mass, M_N is the mass of of the nuclide, which is the number of nucleons A minus the number of electrons, $M_P = m_A - z \cdot m_e$ (the electronic binding energy per electron is excluded). From Krane's derivation of the nuclear binding energy (Krane, chapter 3.3, p. 65).

From equation 3.22, the larger the mass of the outgoing decay channel, the more negative the Q-value will be. Protons (+1 charge) and neutrons (neutral) are the simplest decay channels of the compound nucleus, each carry a spin of 1/2, with masses $m_p = 938.28 \text{ MeV}/c^2$, and $m_n = 939.57 \text{ MeV}/c^2$. Combinations like deuterons ($d=1p+1n$, charge +1) has a mass difference of $\Delta = 2.2 \text{ MeV}/c^2$ from realising 1 proton and 1 neutron separately, a triton ($t=2n+1p$, charge +1) with $\Delta = 8.5 \text{ MeV}/c^2$, 3-Helium (${}^3\text{He}=1n+2p$, charge +2) with $\Delta = 7.7 \text{ MeV}/c^2$ and alpha-particle ($\alpha=2n+2p$, charge +2) with $\Delta = 28.3 \text{ MeV}/c^2$. Thus, Q-values are higher in value, the lighter the particle is. However, in this work, we can clearly see that protons, neutrons and alpha-particles are strongly fed decay channels, while the other don't even appear. The suggested reason for this is that due to **blablabla nuclear physics stuff, like shell structure**, protons and neutrons are favoured, but since the alpha-particle has such a large binding energy, this channel is also favoured.

3.2.2 Deuterons and stopping power

The deuteron consists of a neutron and a proton, and is the simplest bound state of nucleons. Nucleons have an average binding energy per nucleon of 8 MeV. The deuteron with an observed mass value of 2.224 MeV (Krane, p. 81) is a weakly bound. Thus little energy required to break up the deuteron. **does this affect?**

The stopping power of a deuteron beam running through forms the Anderson & Ziegler. **write about Anderson and Ziegler. And how does the stopping power give a flux??**

(Technique nuclear and particle physics p. 30-31): For a particle beam the energy loss is not a continuous process, but collisions based on statistics. A measurement of identical particles will thus show a statistical distribution of ranges centered about the same mean value. This is called range straggeling **this part relevant for describing Ziegler flux??**

Energy straggling: the energy loss distribution: (instrumentation p. 49) "For any given particle however, the energy lost will not be equal to this mean value because of statistical fluctuations which occur in the number of collisions suffered and in the energy transferred in each collision. An initially monoenergetic beam will therefor show a distribution of energy rather than a delta function peak shifted down by the mean energy loss given by the dE/dx formula after passing through a fixed thickness of material.. see if more necessary?"

3.3 Nuclear reaction models

The optical model (proton/neutron, and alpha/deuteron), gamma strength function. **talys 1.9 in reader can contain important info! p. 525.** Optical, gamma-ray strength, compound and preequilibrium. Also read the introduction.

Theoretical nuclear reaction models are important, for both the general understanding of the physics in the data, and to estimate the required cross sections in cases where the data does not make sense or is not available(

EMPIRE 3.2.3

CoH 3.5.3

ALICE 2017

TALYS 1.9

TENDL 2019

3.4 Detection and identification of radionuclides

Gamma-ray spectroscopy is a method to identify and obtain information about radioactive nuclei present in a detector. As beta and alpha decay can result in an excited daughter product, the spectrum in fact shows the de-excitation of the daughter product. Since we know that these gamma-lines are transitions which happens right after a beta or alpha decay (or isomer transition), we identify the parent with gamma-ray spectroscopy. A detector has channels in which counts are registered. These channels are ... similar to the gamma-ray energy. Thus a spectrum has channels (which increases in energy) along the x-axis and counts along the y-axis. If a detector registers many counts, it means that the state is highly populated, and the intensity of the gamma is strong (Krane, p. 351).

Ideally, for all gamma-rays with the same energy, should be detected in the same channel giving a step function. However, realistically, the resolution of a detector is not that good, and instead of seeing a delta peak, the peak is typically gaussian shape with a finite width. The full width half maximum ΔE of the peak tells us how well the relative resolution at gamma-energy E,

$$\text{resolution} = \frac{\Delta E}{E} \quad (3.25)$$

The energy resolution is important, as it tells us how well it can distinguish two close lying peaks from each other (

The peak itself is not directly gaussian. Ionizing radiation statistics is based upon Poisson statistics, where the probability of observing N events is a discrete value

$$P(N) = \frac{\mu^N e^{-\mu}}{N!} \quad (3.26)$$

where μ is the mean value. This distribution counts when the probability is a small (eg decay prob?) value and that the total number of trials are large (number of decays) (

The distribution is not symmetric, but as μ increases in value, the peak approxes a gaussian shape. The total number of counts is the area of the peak. The total peak is a Gaussian assumption but with an exponential skew towards low E caused by incomplete charge collection, and a step function for taking compton background into account.

In calculation of the peak area, there are two uncertainties of relevance, the relative statistical uncertainty in the counting from the Poisson statistics,

$$\sigma N_i = \sqrt{N_i} \quad (3.27)$$

If number of counts $N_i = 10000$, the relative uncertainty ($\frac{\sigma N_i}{N_i} = \frac{1}{\sqrt{N_i}} = 1\%$). Therefor we say that a good number of counts is 10000 or more to reduce the statistical uncertainty. The other is systematic

in the detector, and can for instance be due to a process called annealing, which is heat damage to the detector. Can fix by taking a blanket of resistor wrap crystal in, rise to high temp, let it sit and slowly deheat to room temp, traps will defuse and detector is repaired (this is notes from Andrew).

Also write about deadtime!

3.4.1 Gamma-ray spectrum

Spectrum: consists of photopeaks, a compton continuum, compton edge, backscatter peak, single escape double escape. In cases where positrons exist, chances of having a broad fat 511 keV peak.

Germanium detectors, highest resolution for gamma-rays, from few keV to 10 MeV. The peak to Compton ratio is much greater due to the higher photoelectric cross section of Germanium . The largest challenges are with signal to noise ratio, it is important to shield very well to minimize background radiation (Techniques for Nuclear and particle..... (

here from another citation: "Practical Gamma-ray Spectroscopy". Gordon R. Gilmore. Nuclear Training Services Ltd Warrington UK

The total spectrum can be seen on p. 33 in the book. Pile-up is done because of random summing, determined by the statistical probability of two gamma-rays being detected at the same time and therefore on the sample count rate.

Interaction with detector shielding: Photoelectric effect can be followed by emission of characteristic X-ray of the absorbing medium. X ray can escape the shielding and be detected by the detector. Compton scattering: most gamma rays are scattered through a large angle by the shielding, BACKSCATTERED. Whatever the initial energy was (if scattered by more than 120 degrees) are within 200-300 keV. Peak appears as broad. Pair production: annihilation peak (511 peak) caused by the escape of one of the 511 keV photons from the shielding following annihilation of the pair production positron. Analogous to the single and double escape mechanisms within the detector but only on 511 keV photons can ever be detected since they are emitted in the opposite direction. So in order to have a 511 peak, energy of gamma ray must be more than 1022 keV. (p. 34-35).

The 511 peak can also be expected when positron emitters are present since beta + particle interacts with electron.

Since Compton scattering can be in a spectrum of energies, it gives rise to a Compton continuum, before the gamma-ray escapes the detector.

The shape of the peak: The peak is a histogram that approximates a Gaussian curve (p. 186). Peak searching (SAMPO) using first and second order derivatives to search for peaks (p.185) Due to incomplete charge collection (that electrons or holes are not collected) no matter how it moves counts from the centre of the Gaussian distribution to lower channels, creating a low energy tail to the peak (p.135).

Include a picture of peak shape and gamma-ray spectrum!! from the same book

Chapter 4

Experimental setup

This chapter intends to give a overview of the experimental set-up which was used to obtain cross section measurement. The facility of the Lawrence Berkeley National Laboratory's 88-Inch cyclotron is described in section 4.1. The detector calibration including energy and efficiency is described in section 4.2. The description of the experiment and the stacked target activation method is described in section 4.3, were the characterization and mounting of foils is described in subsection 4.3.1 and the irradiation including tuning of the beam and the intensity profile of the beam is described in subsection 4.3.2. The analysis is described in chapter 5.

4.1 Lawrence Berkeley National Laboratory's 88" Cyclotron

Lawrence Berkeley National Laboratory (LBNL) is a national research laboratory on behalf of the U.S. Department of Energy through its Office of Science, and is operated by University of California, Berkeley. LBNL was founded by Ernest Orlando Lawrence, the inventor of the cyclotron, in 1931.¹. The 88-Inch Cyclotron has a cyclotron number of K=140, and can accelerate both light and heavy ions up to Uranium.². The cyclotron has many purposes, The researchgroup inwhich does isotope production at the facility works with development of nuclear data, along with researching production methods of medically valuable radionuclides (site andrew articles?) But there are multiple programs that takes place in the facility³ which include chip testing and space effects testing, super heavy element searches, fundamental nuclear structure measurements, novel scintillation characterization, fission yield and neutron inelastic scattering measurements (GENESIS) (from Andrew).

A cyclotron is a device that accelerates positively charged particles. It is operated by an alternating (radiofrequency) electric field, and a perpendicular magnetic field, which by the Lorentz Force forces the particle to accelerate in an outward spiral. The 88-Inch cyclotron is an isochronous cyclotron, with a magnetic field that increases with radius. The ions which are accelerated are produced by ECR ion sources and injected into the cyclotron

4.2 Detector calibration

For the gamma-ray spectroscopy, seven different high purity germanium detectors with coaxial right cylinder geometry were used. Six mechanically cooled p-type IDM Ortec detectors (detectors 1-6) with detector diameter 85 mm, detector length 30 mm, hole depth 15 mm, and hole diameter 9 mm, with detector volume 169.996 cm² (assuming detector hole cylindrical). The outside contact layer was doped with lithium, and the hole contact layer with boron. In addition one liquid-nitrogen cooled n-type Germanium detector which also had a thin beryllium window for improved x-ray efficiency (detector 7), with detector diameter 64.9 mm, detector length 57.8 mm, hole diameter 9.4 mm and hole depth 48.6 mm with a detector volume 190.365 cm². The outside contact layer was doped

¹<https://www.lbl.gov/about/>

²<http://cyclotron.lbl.gov/home>

³<https://ieeexplore.ieee.org/abstract/document/7999622/authorsauthors>

with boron and the hole contact layer was doped with lithium. The sketch of the IDM-detector type can be seen in figure 4.2, where J is the hole, which can be seen is not perfectly cylindrical. The detector volumes are comparable....

The high purity Germanium detector is a type of semiconductor, which is a material where the energy required to remove an electron from the valence band (in the outer atomic shell) to the conduction band is small. The germanium atom has atomic number 32, and 4 valence electrons in the outer p4 shell (need citation?). The atoms in the detector are bound through covalent bonds in a crystal structure. The main mechanism of a semiconductor is creation of electron-hole pairs after energy deposition of an ionizing particle in the crystal. If an electron is excited to the conduction band, a hole is left. This hole can move as a neighboring electron fills this spot, leading to a chain reaction, as the hole will move in the crystal. Both the electron in the conduction band and the hole in the valence band contributes to an electric current (

The detectors are doped to create an imbalance in the number of holes and electrons in the conduction band in a pure crystal (

The detector volumes were comparable in size. However, due to the former being broader and shorter, the relative efficiency of the IDM-detectors are larger (ca. 52%) than the germanium detector (ca. 20%). Remember that the geometrical efficiency is dependent on room angle, when surface area is larger then the efficiency is higher. Therefor, the IDM-detectors are more sensitive to background radiation. The IDM-detectors were located in cave 4c (see figure 4.1), which have previously been used as radiation chamber. Thus, background radiation was present. For detector 7, there was led shielding around the detector. In addition, higher resolution. Used for precision measurements, while IDM used for counting and increasing throughput (how many foils can be counted per unit time) Spectra taken on the Germanium detector. The resolution of a detector is defined as the the fwhm of the peak divided by the true gamma. Usually the 1332 keV gammaline of ^{60}Co is used: However we use Cs137 661.657 (keV).... because it is a calibration source. For room131 at 5 cm, 0.25 and for hpge at 10 cm 0.28.

The duration of a voltage pulse signal takes to construct is important, because other events that occurs meanwhile cannot be registered. This leads to a deadtime, which is time where nothing is recorded (

In order to visualize the signal from the detector, Maestro (Multichannel Analyzer Emulation Software⁴) was used.

The electrical signal (voltage pulse) registered in a detector has a net-electrical charge which is proportional to the amount of gamma-ray energy which was registered in the detector (

Here write the equation of peakfit from John as a function of channel number i. But is it the same as in SAMPO??

$$F_{\text{peak}} = m \cdot i + b \dots \quad (4.1)$$

The observed gamma-peaks in the spectra are results of beta-decay where the observed gamma-rays are from the decay of the excited daughter nucleus, or gamma-rays from decay of isomeric states. If two nuclei feeds into the same daughter nucleus, the possibility of sharing excitation level is high. Decay of isomers and ground states can also share multiple gamma-lines as multiple states are populated for the both.

In a detector, the main interactions of gamma-rays and X-rays are via the photoelectric effect, Compton scattering and pair production (

$$\tau \propto \frac{Z^n}{E_{\gamma}^{3.5}}, \quad n = 4, 5 \quad (4.2)$$

As we can see, this effect dominates for detectors with high Z, which is why Germanium semiconductor detectors (Z=32) are preferred over silicone detectors (Z=14). Also, increasing gamma-ray energy

⁴<https://www.ortec-online.com/products/application-software/maestro-mca>

reduces the probability.

In Compton scattering, the photon transfers parts of its energy to an assumed electron at rest, and is scattered with an angle $\theta \in (0^\circ, 180^\circ)$. Dependent on the angle, the energy of the deflected photon will vary, and give a spectrum of different energies. If not all the photon energy is absorbed in the detector, the peak will appear as false an in the Compton continuum. The probability of Compton scattering is proportional to the detector Z-value

$$\sigma \propto Z \quad (4.3)$$

In pair production, the photon is transformed into an electron-positron pair in a nuclear or electric field. Because of this, the energetic threshold is two electron restmasses, of 1.022 MeV. The electron will be registered as an event, and the positron will quickly annihilate with an atomic electron. If both are registered, the peak will appear at the initial gamma-ray energy, if not, we will have a single escape peak at $E_\gamma - 511$ keV or double escape peak at $E_\gamma - 1022$ keV. Probability increases with Z of detector material squared

$$\kappa \propto Z^2 \quad (4.4)$$

(

In addition, interaction via detector shielding can happen, which can lead to emission of characteristic X-rays from absorbing medium. Also, since the shielding material is dense, most gamma-rays from Compton scattering are backscattering, and if scattered by more than 120° appears a broad peak within 200-300 keV. In addition, the annihilation peak at 511 keV appears as either a result of pairproduction in the shielding, where only one gamma-ray will be detected (since they are emitted in oposite directions), or the possibility of annihilation of the postron of a beta+ emitter (Ionizing radiation statistics is based upon Poisson statistics, where the probability of observing N events is a discrete value

$$P(N) = \frac{\mu^N e^{-\mu}}{N!} \quad (4.5)$$

where μ is the mean value, which is equal to the variance ($\mu = \sigma^2$). This distribution is valid when the probability is small (decay probability small?) and the number of trials (number of decays?) are large (

$$\sigma N_i = \sqrt{N_i} \quad (4.6)$$

Therefor, to reduce the statistical uncertainty, a relative uncertainty of less than 1% is preferred ($\frac{\sigma N_i}{N_i} \frac{1}{\sqrt{N_i}} = 1\%$) The systematic uncertainty is in the detector, caused by a process called annealing. write about it??

In this work, the gamma-ray spectra were analyzed in FitzPeaks⁵. The mathematical algorithm inwhich Fitzpeaks in based on is SAMPO80

4.2.1 Energy and peakshape calibration

Since the channel number is not necessarily analogous to the gamma-ray energy, the detector needed to be calibrated. The gamma-ray calibration pointsources ^{137}Cs ($t_{1/2} = 30.08$ years

In FitzPeaks, peak shape and energy calibration was done, by first fitting the calibration spectra taken for each detector, and supplying energy and peak shape source files for the gamma-rays listed in the table for the specific source. This way, each detector was calibrated. For the peak shape, the program optimizes seven parameters; two background peaks, the peak height and location, the peak width, the distance from the peak centroid to the starting point of the exponential tale on either side (

⁵<https://www.jimfitz.co.uk/fitzpeak.htm>

Table 4.1: The calibration point sources along with gamma lines used in the calibration of the detectors. * indicates that the value has been averaged over two peaks with similar energy, less than 1 keV. For the intensity its just added together.

^{137}Cs		^{133}Ba		^{152}Eu	
E_γ	I_γ	E_γ	I_γ	E_γ	I_γ
32.005*	5.63*	53.1622	2.14	121.7817	28.53
36.3405*	1.02*	80.9979	32.9	244.6979	7.55
661.657	85.10	160.6120	0.638	295.9387	0.440
		223.2368	0.453	344.2785	26.5
		276.3989	7.16	367.7891	0.859
		302.8508	18.34	411.1165	2.237
		356.0129	62.05	444.4853*	3.125*
		383.8485	8.94	503.467	0.1524
				586.2648	0.455
				678.623	0.473
				688.670	0.856
				719.353*	0.345*
				778.9045	12.93
				810.451	0.317
				867.380	4.23
				963.712*	14.65*
				1112.076	13.67
				1212.948	1.415
				1299.142	1.633
				1408.013	20.87

4.2.2 Efficiency calibration

The efficiency of the detector is dependent on the shape and density of the detector (

The same calibration point sources which were used in the energycalibration were used in the efficiency calibration, with the same gammas which are listed in table 4.1. The reference date for the sources is January 1st 2009, and the ^{137}Cs measured 38.55 kBq, ^{133}Ba measured 39.89 kBq and ^{152}Eu measured 39.29 kBq, which can also be seen on figure 4.4. Solving Equation 3.15 for effiency, ϵ , the analytical efficiency as a function of gamma-ray energy and intensity is

$$\epsilon(E_\gamma) = \frac{N_C \lambda}{A_0 I_\gamma (1 - e^{-\lambda \Delta t_c}) e^{-\lambda \Delta t_d}} \quad (4.7)$$

where λ is the decay constant and N_C is the number of counts in the measured spectra, and Δt_d is the delay time since the reference date. The analytical efficiency gives one single value for the efficiency at energy E_γ , but we want a continuous function which gives the efficiency at any gamma-energy. A model based upon Gallagher, W. J., Cipolla, S.J. (1974)

$$\epsilon(E_\gamma) = B_0 + \underbrace{(e^{-B_1 E_\gamma^{B_2}})}_{\text{dead layer}} \underbrace{(1 - e^{-B_3 E_\gamma^{B_4}})}_{\text{interacting with volume}} \quad (4.8)$$

where B_i are optimization parameters. The scipy optimize curvefit function

In addition to calibration spectra, long-counted background spectra were taken for each detector, which was later used in the analysis, to verify if gamma-lines were background contaminated.

4.3 The stacked target activation method

The irradiation of the target stack took place on February 26th 2019, and the activated foils were counted on high purity germanium detectors for a total of 4 weeks after end of beam. In addition

to this experiment, two other experiments took place, irradiating strontium with deuterons and a deuteron breakup experiment. The target stack was subject to a 33 MeV deuteron beam, which can be seen in figure 4.5 which from the beamintegrator read of 128.5 nA in beam current. The foils were ca. $25\mu\text{m}$ in thickness and measured approximately 25 by 25 mm in area. The beam was ca. 1 cm in diameter, so the beam was underfilling the targetfoils. Why was it important that the beam was underfilled. On how was this related to the areal densities?

FIND A SOURCE WHICH WRITES MORE!

The stacked-target method originates from Graves et. al. irradiating a stack of thin iron, copper and aluminum foils with a 35-90 MeV protons beam

The stack consisted of natural iridium (99.9%), natural nickel (..), natural copper (..) and natural iron (..) from Goodfellow Corporation, Corapolis, PA 15108, USA. Deuteron-induced products from iridium was the main motivation behind this experiment, primarily because of the potential medically valuable ^{193m}Pt -isomer, and the contribution of nuclear reaction data of the natural iridium (d,x) reactions. For the latter three targets, the well-characterized cross section reactions $^{\text{nat}}\text{Fe(d,x)}^{56}\text{Co}$, $^{\text{nat}}\text{Ni(d,x)}^{61}\text{Cu}^{56,58}\text{Co}$ and $^{\text{nat}}\text{Cu(d,x)}^{62,63,65}\text{Zn}$ from the IAEA monitor database

4.3.1 Characterization of the target foils

The iridium foils were bought in 25 by 25 mm squares, and the copper, iron and nickel foils were cut into approximately 25 by 25 mm squares, where each foil was cut from the same sample. The length of each foil along each side and the thickness was measured with a caliper (Mitutoyo Absoule Digimatic) and a gauge caliper (Mitutoyo IP65 Coolant Proof) respectively. An analytical balance weight (Mettler Toledo) was used to measure the mass of each foil which was prewashed with isopropanol to clear the foils from surface contamination. Each unit was measured four times, and the values listed in table 4.2 are the averaged measurements. The mass density was calculated for each foil which was calculated using the average mass of each foil, divided by the averaged area. The uncertainty in the areal density was calculated as the standard deviation of the data described in equation A.2. The areal densities were later in the analysis converted to number of nuclei per cm^2 , which was done numerically multiplying the mass density with Avogadro's number, and dividing by the mol-mass of the target atoms. The measured thicknesses were not used in the analysis, but was a confirmation that the foils were ca. $25\mu\text{m}$ in thickness. The measured values varied from $24.3\mu\text{m}$ (Ir03) to $34.8\mu\text{m}$ (Cu02), which were within accepted values.

After the characterization, each foil was mounted on ca. 1.6 mm thick plastic frames over a hollow center and attached with 3M 5413-Series Kapton polyimide film?? tape along the edges. From previous experiments, the Kapton tape has been used to seal the foils into airtight pockets for foil containment, but has appeared to have an impact on the proton stopping power

4.3.2 Irradiation

The tuning the beam

Before irradiation, the deuteron beam was tuned to be ca. 1 cm in diameter. In addition, the experiments taking place simultaneously demanded a precise position of the beamspot since the target size were in the order of the beamspot. The beam spot was first visualized using a ca. 2.5 cm thick borosilicate glass, painted with a mixture of phosphor powder and vacuum grease (so that the paint does not evaporate as the tube was pumped down to vacuum). When ionizing radiation strikes the phosphor, the phosphor is excited and emits light in the de-excitation, called phosphorescence. The glass was placed on the end of the beam tube. With a camera placed in cave 0, from the control room, the beam spot could be visualized, and could be steered to be centered and ca. 1 cm in diameter. The beamspot can be visualized in figure 4.7 (left), and the borosilicate glass placed on the end of the beam tube can be seen in figure 4.7 (right). Secondly, the beam had to be constant over the target stack, i.e. not diverge or converge. Gafchromic films were placed in the front and the back of the target holder, separated by the spring. The films were exposed for a brief second, and the blue spot on the developed film was evaluated. This was done until the beamspot was good both in the front

Table 4.2: Characterization of each foil, along with calculated mass density. Each length is measured in mm, and mass in grams. *: measured from previous experiments

Foil	Length1 (mm)	Length2 (mm)	Thickness (mm)	Mass (g)	Mass density (mg/cm ²)
SS1	100.199*				
Ni01	25.228	25.293	0.0285	0.1453	22.772 ± 0.138
Ir01	24.943	24.968	0.0295	0.3436	55.174 ± 0.053
Cu01	25.553	24.883	0.0341	0.1420	22.338 ± 0.048
Fe01	24.400	26.068	0.0278	0.1274	20.030 ± 0.110
Ni02	25.288	25.428	0.0295	0.1487	23.118 ± 0.096
Ir02	24.923	25.005	0.0278	0.3465	55.601 ± 0.238
Cu02	25.443	25.550	0.0348	0.1451	22.325 ± 0.028
Fe02	25.525	23.800	0.0274	0.1216	20.017 ± 0.034
Ni03	25.295	25.210	0.0270	0.1425	22.338 ± 0.066
Ir03	24.885	24.983	0.0243	0.3459	55.643 ± 0.121
Cu03	25.560	25.508	0.0343	0.1455	22.313 ± 0.043
Fe03	26.113	25.235	0.0310	0.1315	19.948 ± 0.114
Ni04	25.303	24.888	0.0273	0.1304	20.704 ± 0.068
Ir04	24.960	24.833	0.0261	0.3471	56.000 ± 0.109
Cu04	25.153	25.603	0.0333	0.1435	22.284 ± 0.027
Ni05	25.325	25.495	0.0263	0.1406	21.768 ± 0.045
Ir05	24.948	24.958	0.0256	0.3435	55.161 ± 0.081
Cu05	25.213	25.573	0.0334	0.1447	22.443 ± 0.028
Ni06	25.530	25.195	0.0285	0.1471	22.861 ± 0.123
Ir06	24.760	24.960	0.0240	0.3444	55.731 ± 0.088
Cu06	25.343	25.513	0.0340	0.1448	22.396 ± 0.012
Ni07	25.338	25.278	0.0268	0.1479	23.092 ± 0.078
Ir07	24.955	25.008	0.0278	0.3538	56.685 ± 0.085
Cu07	25.625	25.248	0.0326	0.1444	22.320 ± 0.014
Ni08	25.205	24.950	0.0256	0.1409	22.409 ± 0.124
Ir08	24.723	24.985	0.0281	0.3585	58.030 ± 0.130
Cu08	25.370	24.885	0.0333	0.1414	22.401 ± 0.033
Ni09	25.220	25.378	0.0257	0.1392	21.741 ± 0.073
Ir09	24.670	24.993	0.0273	0.3494	56.669 ± 0.043
Cu09	25.390	26.455	0.0331	0.1506	22.425 ± 0.041
Ni10	25.285	24.405	0.0271	0.1425	23.093 ± 0.024
Ir10	24.973	24.980	0.0270	0.3435	55.065 ± 0.055
Cu10	25.470	25.338	0.0355	0.1440	22.314 ± 0.047
SS2	100.865*				
P-degrader	1900.0*				
Ni neutron monitor	?				

and in the back of the stack. The Gafchromic films after direct exposure can be seen in figure 4.8 in the target holder.

The beam efficiency transmission was calculated by measuring the current at the Faraday cup right after the cyclotron vault (BS-02) and right before cave 0 (FC-01). BS-02 was measured to be 420 nA and FC-01 was measured to be 285 nA. This gave beam efficiency of transmission

$$\frac{FC - 01}{BS - 02} = 67\%$$

Irradiation of the target stack

The irradiation lasted for one hour. The number of charges collected?? was registered off the current integrator on the electrically isolated beamline, and registered evenly to ensure that the beamcurrent was more or less constant throughout the irradiation. After exactly one hour, the beam integrator read of $I\Delta t = 2314$ C, with full-scale amperes being $2 \cdot 10^{-7}$ A. The average beam current hitting the

front of the stack was thus

$$\frac{2314 \cdot 2 \cdot 10^{-7}}{3600} = 128.5 \text{ nA} \quad (4.9)$$

Before the beam was turned on, the beam tube had to be pumped down to a vacuum, to not attenuate the beam. The targetholder was placed in the end of the beam tube (**mounts of the end of an electrically-isolated beamline, (iron paper andrew)**). Figure 4.9 shows how the targetholder was placed in the end of the beam tube. About ten minutes after end of beam, cave 0 was opened, and the targets were sealed in plastic bags to avoid contamination. The iridium foils counted from 15 minutes after end of beam on detector 7, and the other foils following up shortly after. All the foils were counted for ca. four weeks following end of beam on the various detectors, with short counts in the beginning to have good statistical data for the short-lived activities, and longer and longer counts as the shorter and medium-lived activities decayed out, to have good statistics (enough counts). The counts were done as jobscripts in the beginning, so that the same foil was measured multiple times, and the gamma-lines were observed multiple times over short counts rather than one long count. The reason why the foils were counted multiple times was to reduce the statistical uncertainty, and in addition make sure that the products with similar gamma-lines but different half-lives were observed independently if possible. Since the detectors were calibrated at various distances, the deadtime of the foils right after end of beam could be reduced, however, as high as 16-22% deadtime was present, but reduced to less than 5% within a cooling time of ca. 1 day after end of beam **double check, but on quick overview this seemed right.** ^{193m}Pt has one single weak gamma-line at 135.5 keV (0.11%). In addition, it is located at the shoulder of ^{192}Ir at 136.39 (0.199%). The half-life of ^{192}Ir is long, and it was important to make sure that the two peaks were identified independently. Due to the relatively long half-life of ^{193m}Pt , and the weak gamma-ray, it was made sure that the single gamma-line was observed within a few days after end of beam, when the counts were longer.

Intensity profile of the beam

After irradiation, Gafchromic film were attached to the activated stainless steel in the front and the back of the stack, to obtain a spatial intensity profile of the beam. The activated film attached to the Gafchromic film can be seen in figure 4.10. The radius of the activity from stainless on gafchromic film was used in the imaging process program ImageJ-1.52k, which is developed by the National Institutes of Health and the Laboratory for Optical and Computational Instrumentation (wiki, imageJ). The gafchromic films were scanned alongside a ruler for scale comparison. Since the images are divided into pixels, a 3 (**why 3cm?**) cm linesegment was drawn alongside the ruler to set the scale to pixels/cm in the program. The intensity over the developed film was obtained by inverting the scanned image, and drawing a line segment along the beam spot that created a position dependent intensity array. The intensity profile can be fitted to a Gaussian, which is shown examplewise in figure 4.11, which is the horizontal beam profile in the front and the back of the stack. In the assumption that the beam was underfilled, it was important to build confidence in that the beamspot was ca. 1 cm in diameter, which was done estimating the full width half maximum of the Gaussian profile. The FWHM over SS1 was 1.2017 cm horizontally ($\sigma^2 = 0.2604 \text{ cm}^2$) and 1.1420 cm vertically ($\sigma^2 = 0.2352 \text{ cm}^2$). The FWHM over SS2 was 0.6706 cm horizontally ($\sigma^2 = 0.0811 \text{ cm}^2$) and 0.5783 cm vertically ($\sigma^2 = 0.0603 \text{ cm}^2$).

Normally the beam broadens throughout the stack due to scattering. As we can see, this is not the case, since the beam is stopped in the targetstack, and therefore we do not know how much the beam truly scatters. This gives a higher uncertainty. The stainless steel (which consists of ..) has fast decay time. However since it emits beta-particles, the radius will slightly increase, and the true beam spot is slightly smaller. Thus the estimated FWHM values for SS1 seems to be within the criterion for underfilled targets.

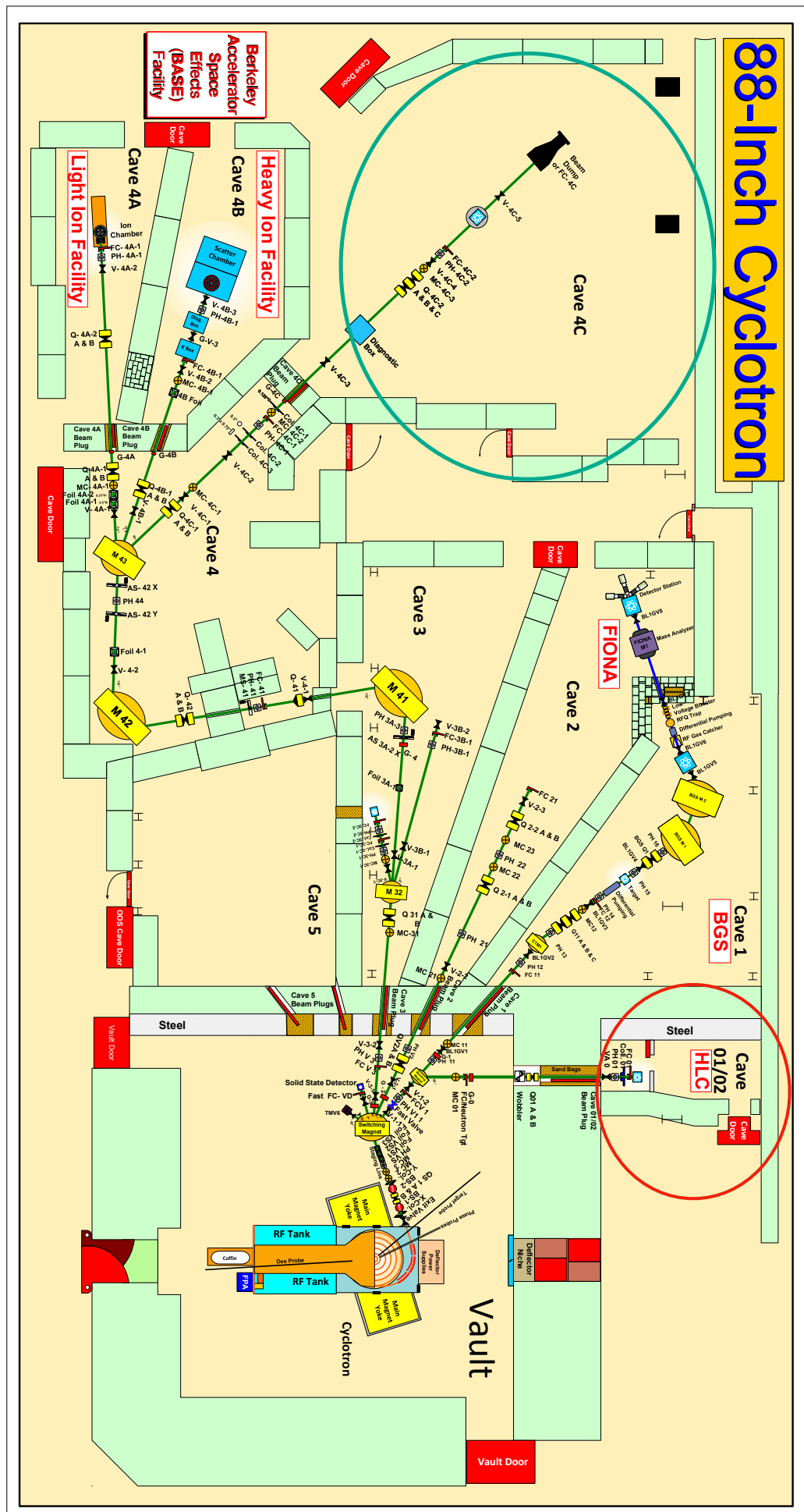


Figure 4.1: An overview of the 88" Cyclotron facility. The facility have several isolated beamlines that can be used for irradiation in the experimental caves. The irradiation of the target stack took place in cave 01/02 (red circle), while some of the detectors used in the gamma-rays spectroscopy was located in cave 4C (green circle) which is no longer used as an irradiated chamber. Bending magnets are used to steer the beam in the cyclotron vault, and focusing quadrupole magnets are used to focus the beam in the cyclotron vault.

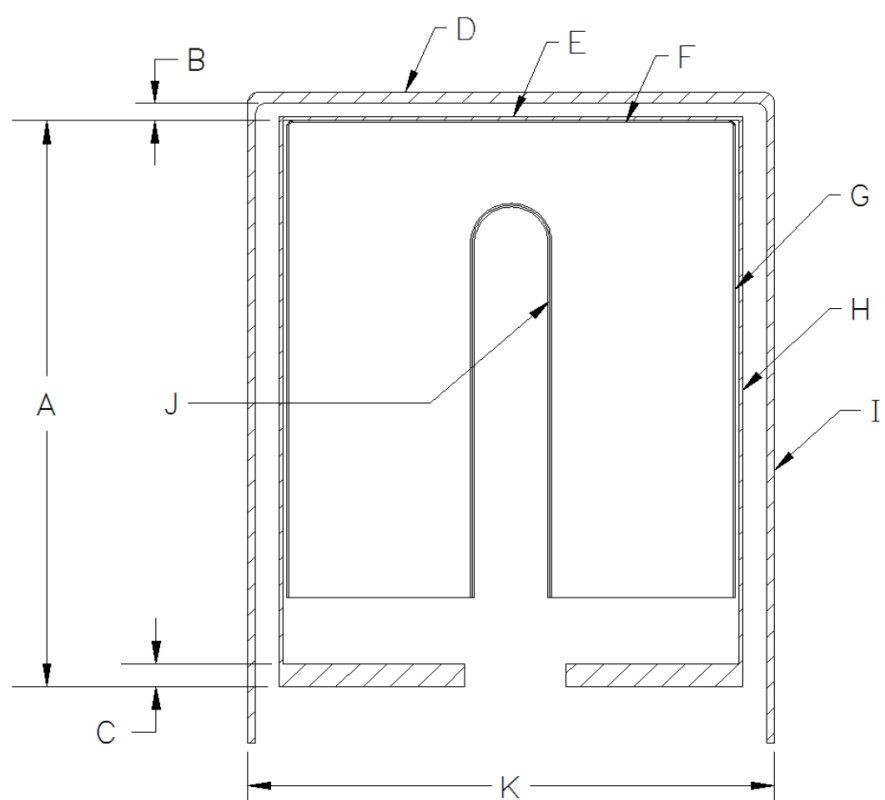


Figure 4.2: The figure shows a scetch of the detector. The figure is from the detector diagram of IDM.

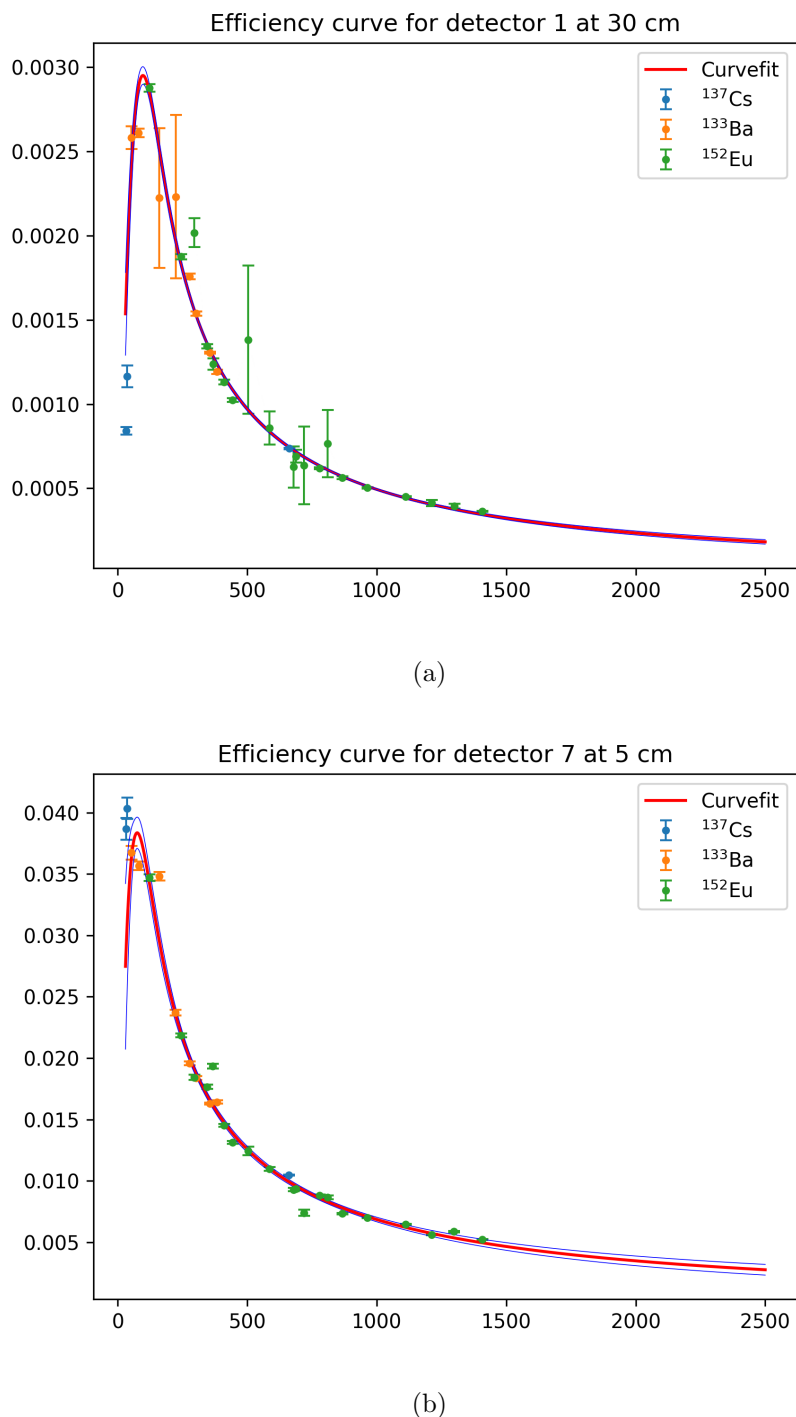


Figure 4.3: Two examples of efficiency curves. **top:** The efficiency curve of detector 1 at 30 cm which is located in cave 4C, and has a lower detector volume along with a different shape. **bottom:** The efficiency curve of detector 7 at 5 cm is located in a separate room and had led shielding. The geometry shape is better here!



Figure 4.4: The calibration point sources that were used in the efficiency calibration of the detector. (^{22}Na was excluded because it was difficult to work with.)

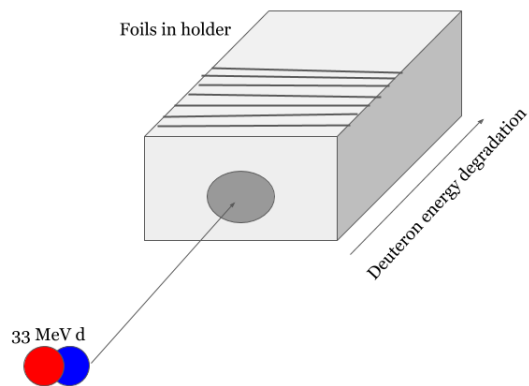


Figure 4.5: The fundamental idea of the experiment where a stack of targets are placed in a target holder, and irradiated with accelerated 33 MeV deuterons. As the energy degrades through the beam stack, it is possible to have multiple cross section measurements at different energies.

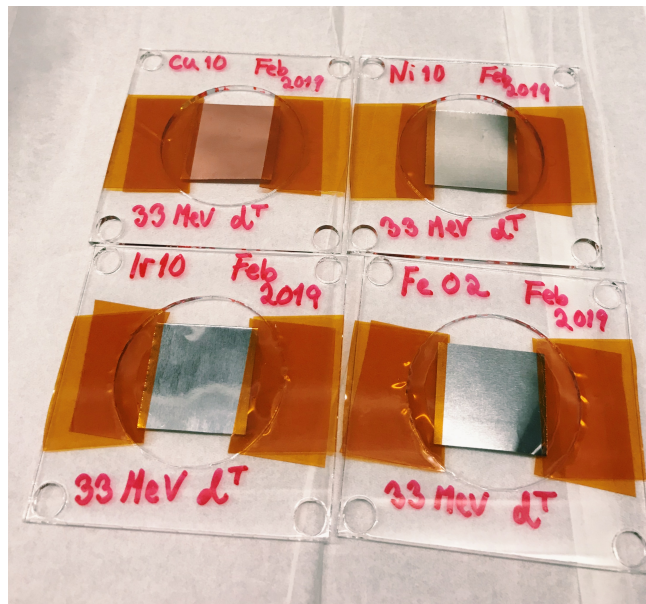


Figure 4.6: The figure shows the four different targets mounted on plastic frames with capton tape attached along the edges of the foils.

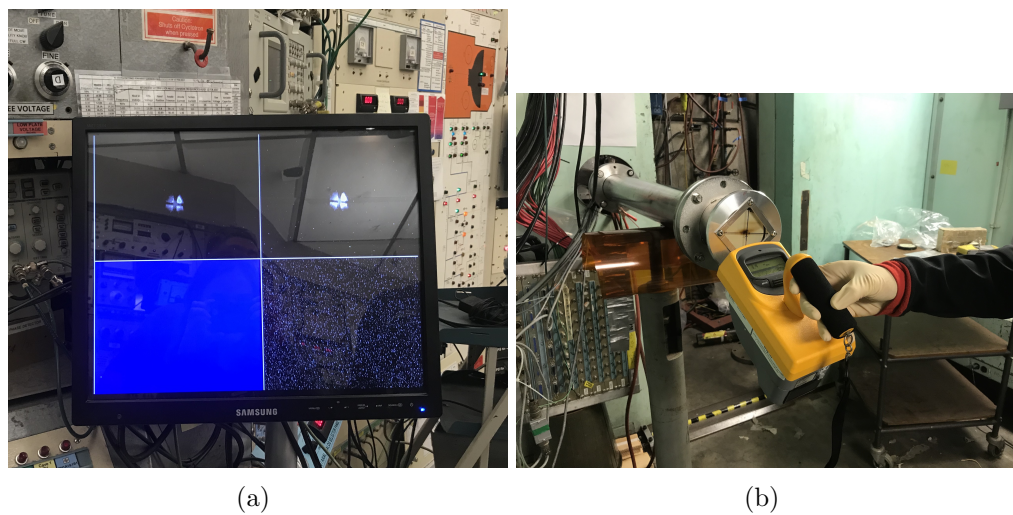


Figure 4.7: The figure shows the beamspot which could be visualized from the control room, and the borosilicate glass placed on the end of the beam tube. The dose present after the beam was on was always measured.

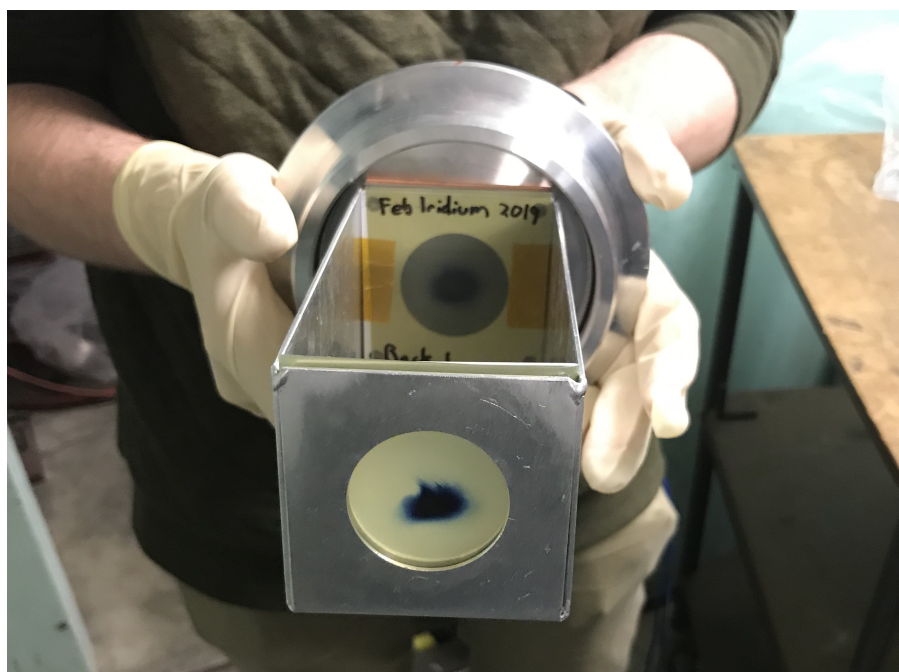
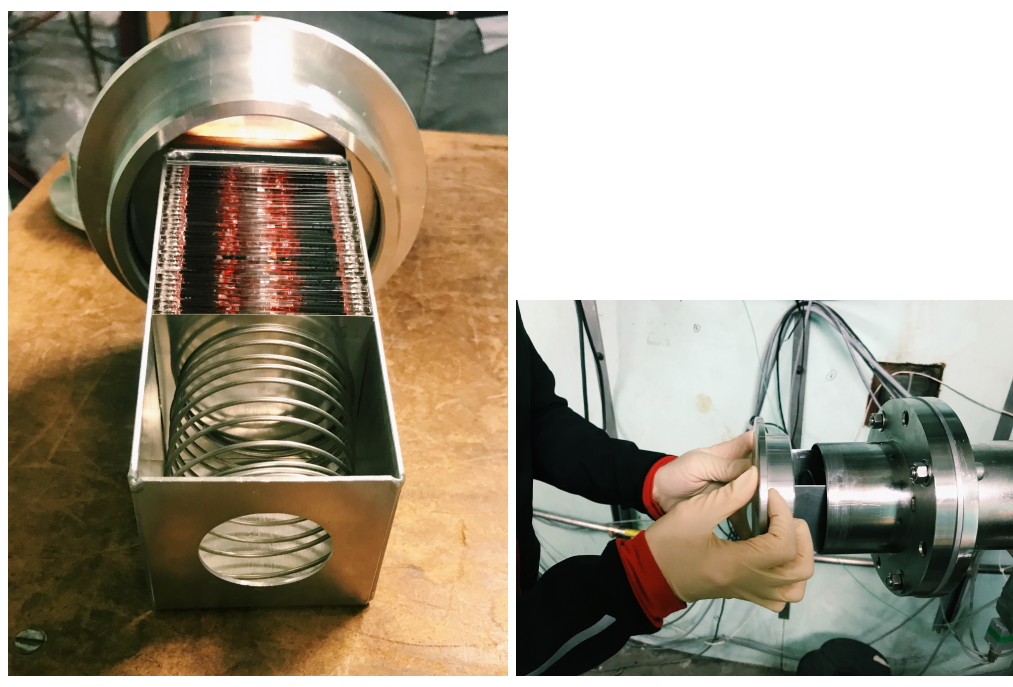


Figure 4.8: The gafchromic films were exposed for a brief second



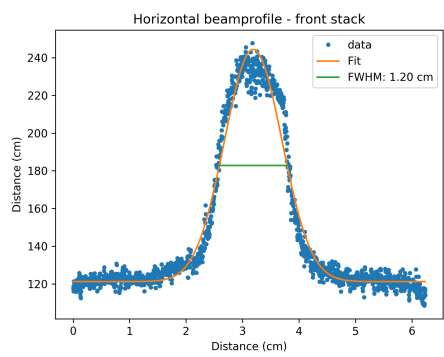
(a) The target stack in target holder

(b) Target holder placed in the end of beam tube

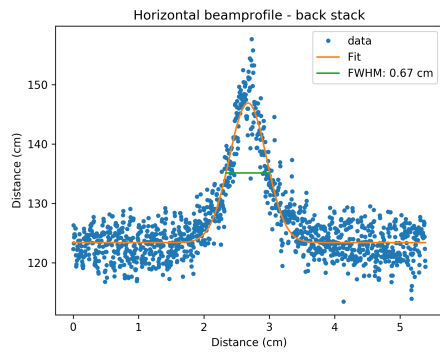
Figure 4.9: Figure shows the target stack and how it was placed in the beam tube.



Figure 4.10: The gafchromic film on the activated SS1 foil.



(a) Horizontal intensity profile of SS1



(b) Horizontal intensity profile at SS2

Figure 4.11: Figure shows the intensity profile of the deuteron beam in the front and in the back of the stack horizontally.

Chapter 5

Analysis

The equation which is used to find the reaction cross section of a product nucleus is given in equation 3.18, where A_0 is the end of beam activities which are described in section 5.1, t_{irr} is the irradiation time which was one hour, where N_T is the number of target nuclei, which is the areal density measured in table 4.2, $\Phi(E)$ is the deuteron beam current which is described in section 5.3 and λ is the decay constant for the product nucleus. The final cross section results are represented in the next chapter.

5.1 Analyzing the gamma-ray spectra

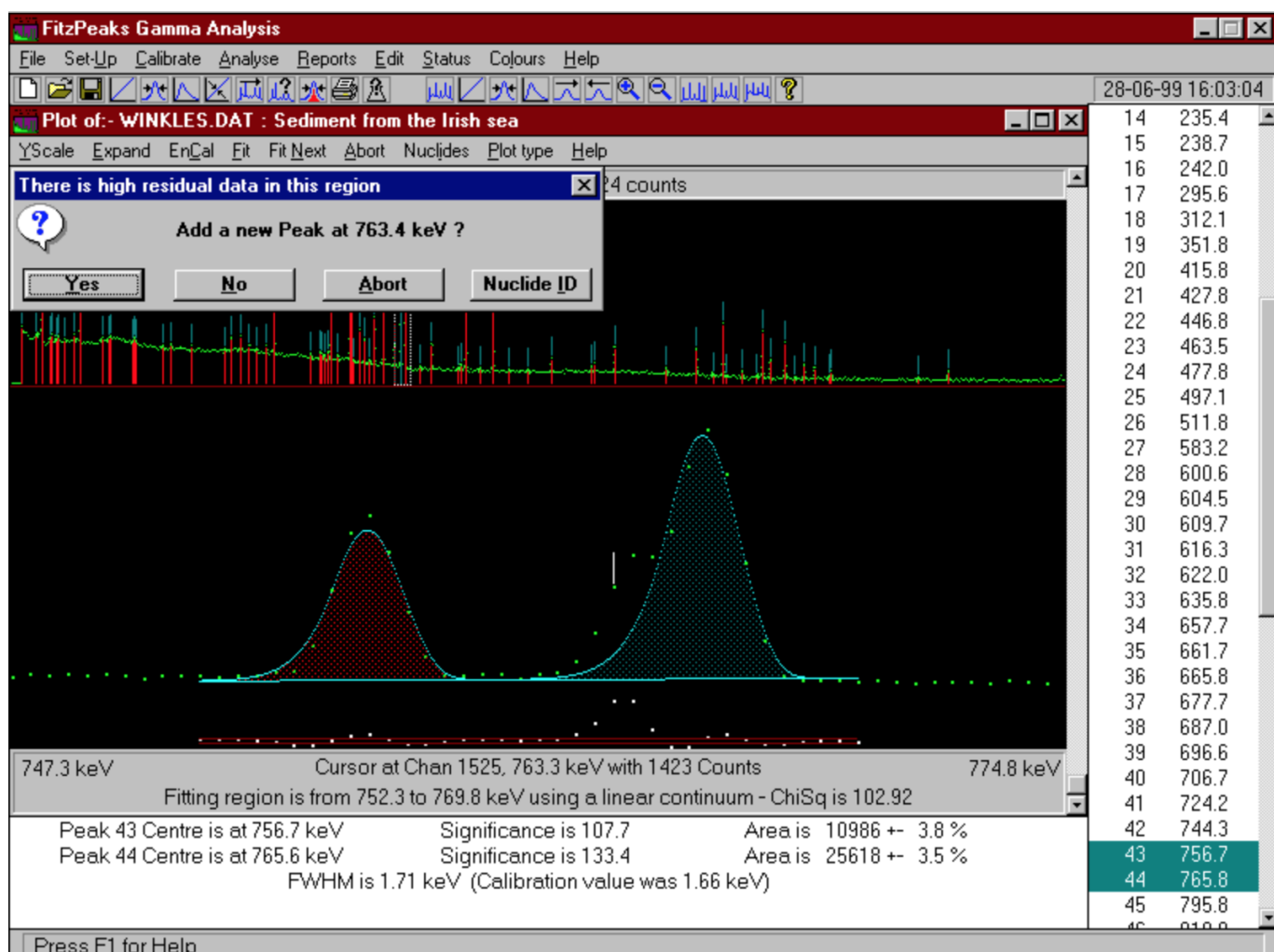
The gamma-ray spectra were analyzed in FitzPeaks, as there were more than 300 spectra and it would take too long time to do this independently. As described in section 4.2.1, the method in which the algorithm searches for peaks are through the second derivative. The peak areas were calculated by fitting the precalibrated modified Gaussian to the data with a weighted least squares formula using a parabolic background. how was the peak area uncertainties calculated? The fitting parameters were determined automatically by the program, and peaks separated by less than 4 times the average full-width half-maximum are fitted together

Figure 5.3 shows the X-ray region and gamma region of ^{193m}Pt , where.....

For each spectra a report file containing peak energy, centre channel, full width half maximum, significance, goodness of fit, peak area and uncertainty in peak area, gammas per second and uncertainty in gammas per second and a background estimation for each peak was provided. The parameters which were used in the analysis was the peak energy for identification, the peak area N_C which was used in the activity equation 3.15 and estimation of efficiency, and uncertainty in peak area. The gammas per second (also called countrate) was used to get an indication of the rate of gammas, which were used as a critical tool to evaluate background contamination in a peak, by comparement to background spectra.

A matlabscript written by Voyles, A. (2019) was used to loop over all report files for each single spectra in each foil. Gamma-energies with less than 0.5 (doublecheck) keV in difference were added and averaged, which can be seen on figure 5.4 where the channel number is listed on the x-axis and the gamma-ray energy is listed on the y-axis. The result is a staircase where the energies within the tolerance are averaged. This gave a list of gamma-ray energies for each target foil type, one for iridium, one for nickel, one for copper and one for iron. Each of the gamma-lines were identified manually, going through possible reactions based on Q-value. If more than one nucleus fed into the same gamma-ray energy within a tolerance of 1 keV, then the peak was not used if there were other possible gamma-ray energies to take from. If not, the half-lives were compared, and if there was a large difference, only early spectra or very late spectra were used when the activity of the other was not present. In addition, peaks which were contaminated with background radiation was also not used, unless the countrate was very small in comparison to the countrate of the peak. If it had to be used, the method for background subtraction is described below.

For each nucleus identified, the gamma-rays from nndc (listed in tables B.1, B.2, B.3 and B.4 for nickel, iron, copper and iridium respectively) along with half-life, intensity and uncertainty in intensity were gathered.

Figure 5.1: from:<http://www.jimfitz.co.uk/pk1fsz.htm>

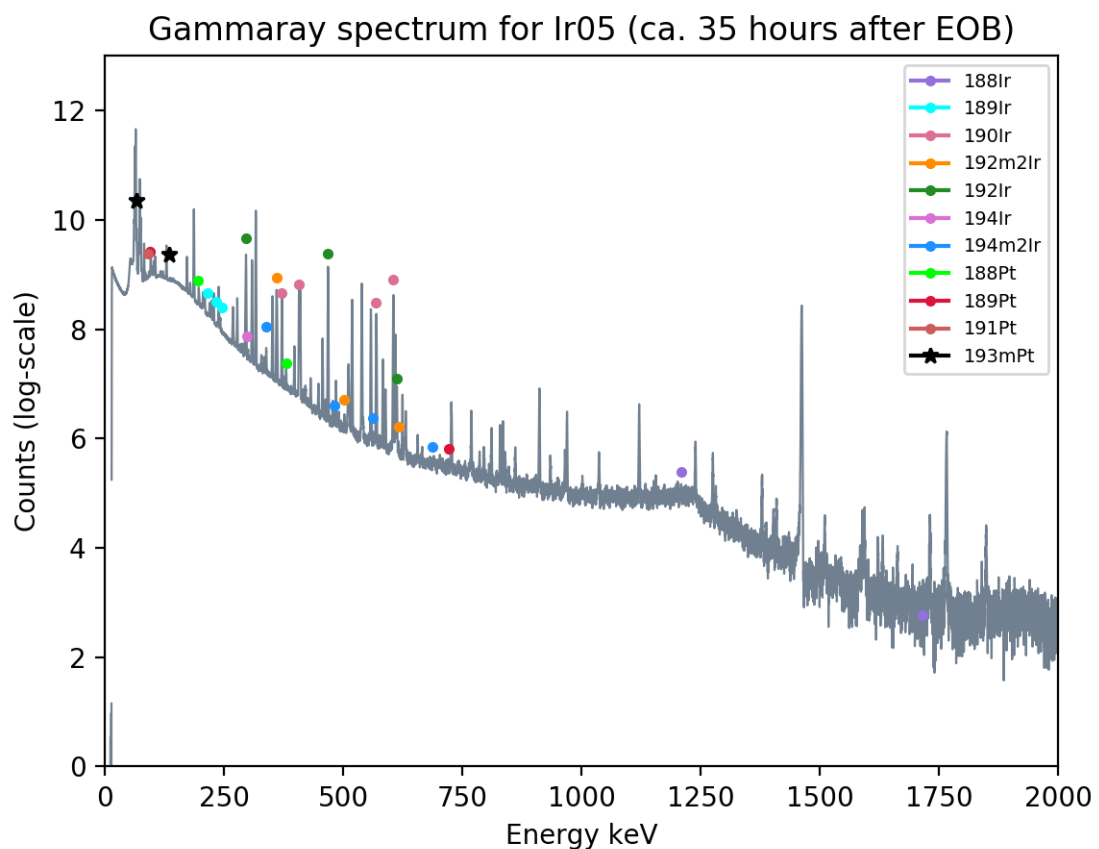


Figure 5.2: Gammaray spectrum for Ir05 taken approximately 35 hours after end of beam. Nuclei does not necessarily represent what is present in the spectrum, but where the peak would have been. Hard to include all since there are different decay times. **right:** the total, **left:**zoomed to show the staircase

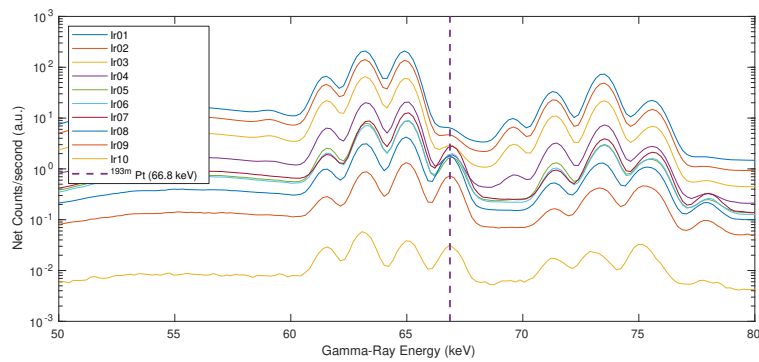
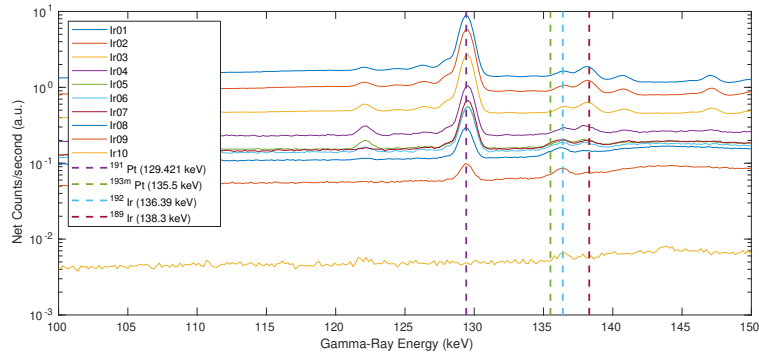

 (a) X ray plot of ^{193}mPt .

 (b) Gammaphot of ^{193}mPt

Figure 5.3: Which spectra are these??

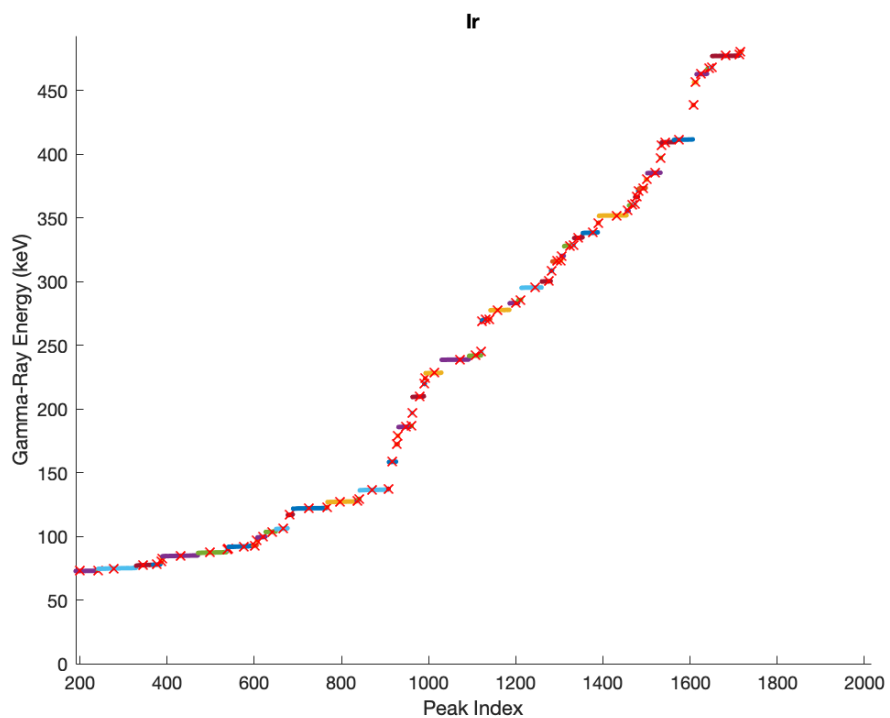


Figure 5.4: Zoomed staircase for energies between 0 and ca. 500 keV. Shows how the gamma-rays within a tolerance of 0.5 keV were averaged. Each "staircase" represents one gamma-ray energy which was used for identification.

5.1.1 Background subtraction

In a few number of cases, background subtraction was necessary due to the presence of some nuclei in the background, which was only problematic for the detectors located in cave 4C. Nuclei of cobalt was in particular present in the background. The general rule of thumb was only to use background subtraction when all gamma-lines of the nucleus was contaminated with a countrate of the same order. If not, the line was avoided.

The countrate is defined as the number of counts divided by the livetime of the spectrum, in units counts/second

$$C = \frac{N_C}{\Delta t_{\text{live}}} \quad (5.1)$$

The number of true counts is the sum of the true gammas and the background

$$C_{\text{true}} = C_{\text{obs}} - C_{bg} \quad (5.2)$$

The countrate in the background spectra are constant, which here is denoted as C_{bg} . The observed countrate is thus the number of true counts divided by the livetime of the spectrum and the background countrate on the detector. From equation 5.1, the number of counts are the countrate multiplied by the livetime, which gives

$$N_{\text{true}} = N_{\text{obs}} - (\Delta t_{\text{live}} C_{bg}) \quad (5.3)$$

5.2 End of beam activities

The end of beam activities were estimated by extrapolating backwards in time with the measured activities at various timepoints after the end of beam. The activities measured in each spectrum as a function of time since end of beam was calculated using equation 3.14 along with a self-attenuation correction:

$$A(\Delta t_d) = \frac{N_C \lambda}{\epsilon_\gamma (1 - e^{-\lambda \Delta t_d}) e^{-\mu \rho \Delta r / 2}} \quad (5.4)$$

where μ is the photon attenuation coefficients from the XCOM photon cross section database¹, and $\rho \Delta r$ is the areal density of the foil. The gammas which were used are listed in tables B.2, B.1, B.3 and B.4 for iron, nickel, copper and iridium respectively. The gamma-ray self-attenuation (which is typically less than 0.2 % (Iron paper, Andrew)) correction is based on the assumption that all activity that is made is located midway in the foil thicknesses. In reality however, the activity profile will follow the same shape as the excitation function over the energy range that expands over the foil, if we assume that the stopping power $dE/dx=0$ which is a good estimation for thin foils less than 100 mg/cm²? (since activity and cross section are proportional). We do not know the excitation function ahead of time, and the excitation function does not change much either, since the foil thicknesses are so thin. So instead, this simplification is done, assuming that the average attenuation is through half of the foil thickness.

In a matlabscript written by Voyles, A. S (2020), the gamma-ray energies used, and intensity, uncertainty in intensity and half-life (listed in table products..) were assigned to the nucleus. Each foil type and foil number was looped over to see if the observed gamma-ray within a tolerance of 1 keV was registered, and with the number of counts, uncertainty in number of counts, the time since end of beam, the areal density and mass attenuation correction, and the efficiency which was dependent on which detector, the activity at each observed timepoint since end of beam was calculted accordint to equation 5.4. The result was an output file for each foil with the calculated activity according to

¹<https://www.nist.gov/pml/xcom-photon-cross-sections-database>

equation 5.4 with hours since end of beam. The output files were read into a separate program for calculation of the end of beam activities.

The equation describing the shape of the decay curve is given in equation 3.3 for single decay or 3.4 for multiple decay. Decay chains of single and two-step decay ($n=1,2$) was sufficient in this analysis;

$$A = A_0 e^{-\lambda \Delta t_d}, \quad \text{single step decay} \quad (5.5)$$

and

$$A_2(t) = \lambda_n \left[A_{1,0} \lambda_1 \frac{(e^{-\lambda_1} + e^{-\lambda_2})}{\lambda_1 - \lambda_2} + A_{2,0} e^{-\lambda_2 t} \right], \quad \text{two step decay} \quad (5.6)$$

where subnumber 1 is the parent nucleus, and subnumber 2 is the daughter nucleus. Parent activity is calculated from single step decay.

The extrapolation was done using the scipy optimize curvefit function

For the latter, the two optimizing parameters are correlated, and equation A.6 had to be used for the uncertainty.

Figure 5.5 shows three examples of the three different activity curves; one step decay for ^{193m}Pt ($t_{1/2}=4.33$ days), two step decay for ^{58}Co ($t_{1/2}=70.86$ days) with feeding from the isomer ^{58m}Co ($t_{1/2}=9.10$ hours), which had to be fitted using two optimizing parameters, and twostep decay of ^{56}Co ($t_{1/2}=77.236$ d) with feeding from ^{56}Ni ($t_{1/2}=6.075$ d) using the activity of ^{56}Ni and the optimized parameter of ^{56}Co . The uncertainty bands are large for ^{58}Co , as the twostep decay with no observed parent contributes to a higher uncertainty.

5.3 Deuteron beam current and energy assignment

The beamintegrator measured a current of 128.5 nA in front of the beam stack. However in order to have precise cross section measurements, the nominal beam current in each foil was calculated. The IAEA recommended monitor reactions (2017) $^{nat}\text{Ni(d,x)}^{61}\text{Cu}, 56, 58\text{Co}$, $^{nat}\text{Cu(d,x)}^{62,63,65}\text{Zn}$ and $^{nat}\text{Fe(d,x)}^{56}\text{Co}$

$$\Phi(E) = \frac{A_0}{N_T \sigma(E)_{\text{mon}} (1 - e^{-\lambda \Delta t_{\text{irr}}})} \quad (5.7)$$

Equation 5.10 builds upon the thin target assumption, which implies that the energy degradation in the foil is zero. However, we know that there is an energy distribution, which was estimated using NPAT's (Nuclear Physics Analysis Tool) Ziegler simulation². The ziegler code simulates the deuteron transport based upon the Anderson & Ziegler stoppingpower mode

$$\langle E \rangle = \frac{\int E \frac{d\phi}{dE} dE}{\int \frac{d\phi}{dE} dE} \quad (5.8)$$

The uncertainty in beam energy is divided into low energy and high energy tale, with the FWHM split by the centroid (figure 5.9).

Likewise, the energydependent monitor IAEA cross sections need to be flux-weighted over each foil. In order to do this, a spline interpolation over the energy array over each foil provided by the Ziegler simulation was spline interpolated with the IAEA recommended cross section data. Thus, the monitor cross section in equation 5.10 is modified to

$$\sigma(\langle E \rangle) = \frac{\int \sigma_{\text{mon}} \frac{d\phi}{dE} dE}{\int \frac{d\phi}{dE} dE} \quad (5.9)$$

²John's code, must cite.

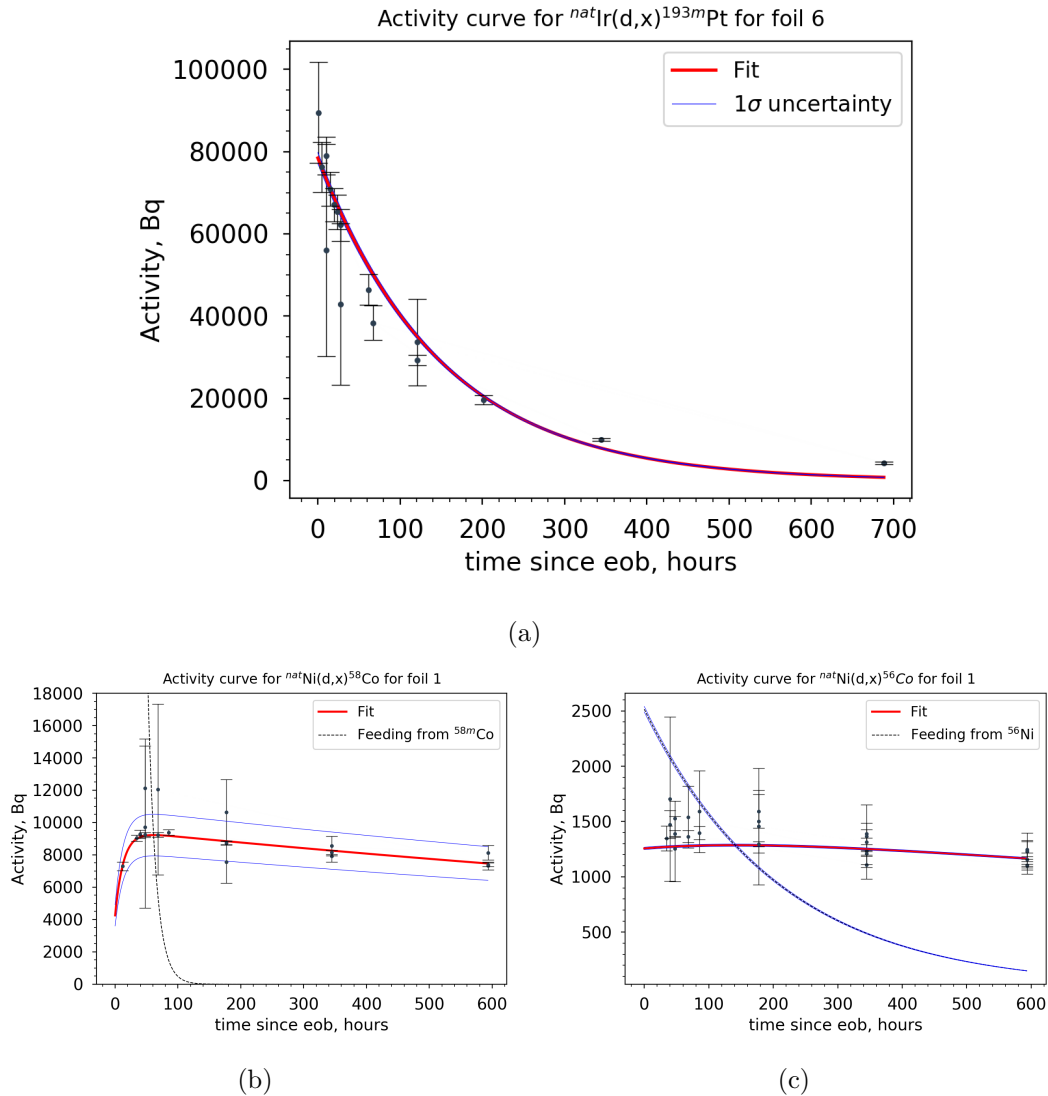


Figure 5.5: Examples of three activity curves. **Top:** Onestep decay for ^{193m}Pt ($t_{1/2}=4.33$ days), extrapolated with equation 5.5. **Bottom left:** Twostep decay for ^{58}Co ($t_{1/2}=70.86$ d) with feeding from the isomer ($t_{1/2}=9.10$ h, IT:100%). The curve was extrapolated using twostep decay (equation 5.6) with both daughter and parent as optimizing parameters. **Bottom right:** Twostep decay for ^{56}Co ($t_{1/2}=77.236$ d) with feeding from ^{56}Ni ($t_{1/2}=6.075$ d, ϵ :100%).

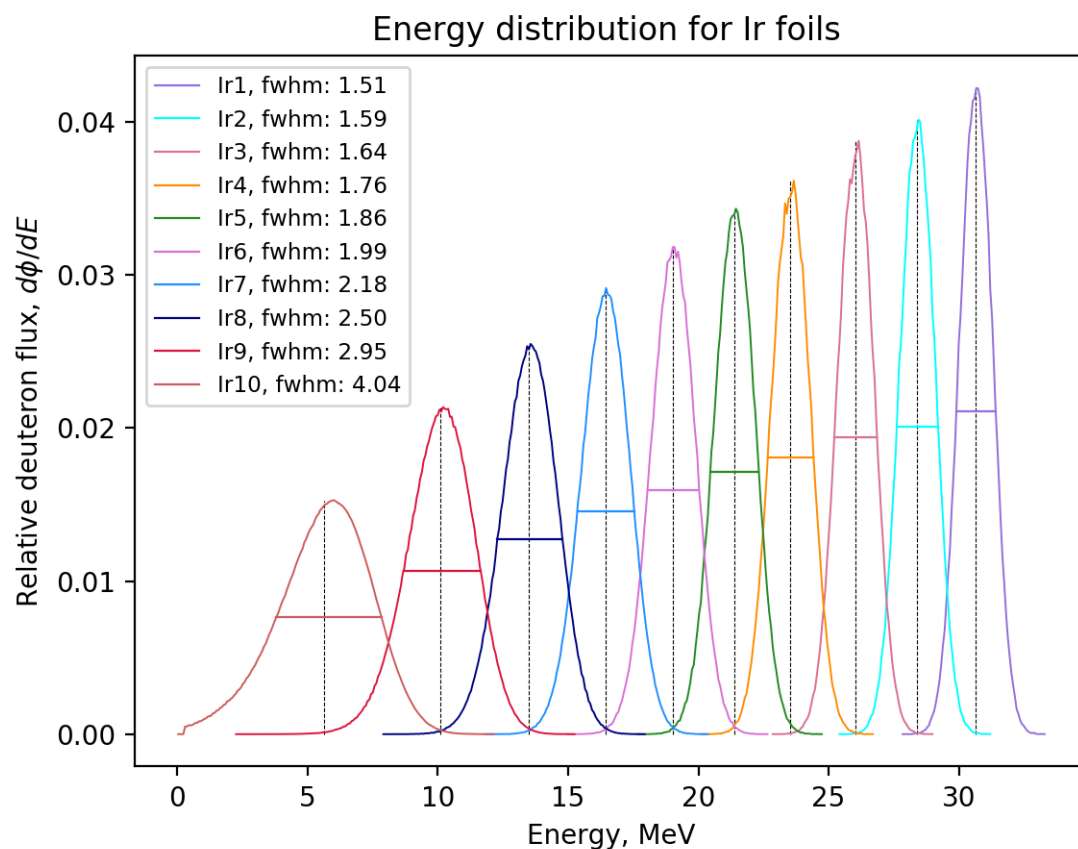


Figure 5.6: Iridium energy flux distribution over the 10 foils. As the energy degrades, skewed and larger full width half max. The vertical line in each peak is the mean value. This indicates that at lower energies, the right uncertainty is greater than the left uncertainty in the peak.

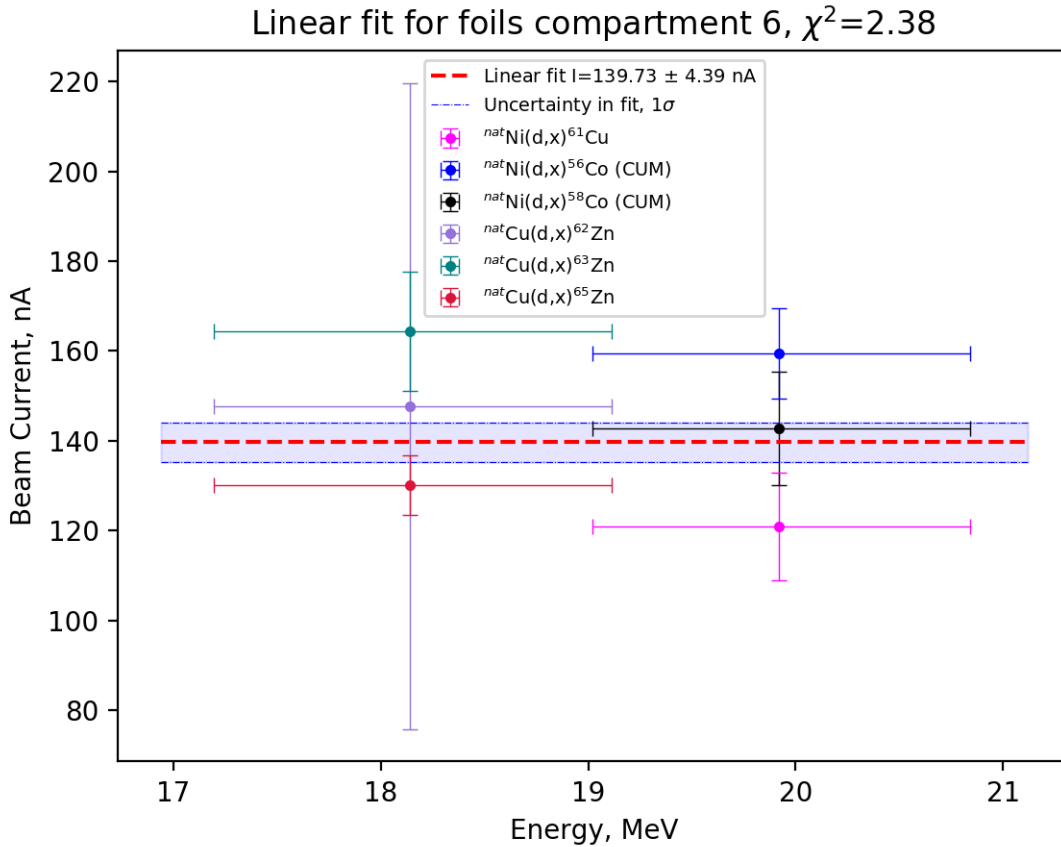


Figure 5.7: The estimated (uncertainty weighted) beamcurrent over compartment 6.

5.3.1 Variance minimization for the deuteron transport calculations

In theory, the estimated beam current of a charge particle beam should be constant, until completely stopped, since the majority of the incident particles does not interact in nuclear reactions, but only lose energy via elastic and inelastic scattering. However, non-consistant values of the beam current, especially in the back of the stack can be due to energy bins being assigned wrongly in the energy distribution simulation done in Ziegler or a systematic error in the areal density which gets progressively worse further back in the stack (Niobium paper, Andrew). A way to work around these errors was to perform a variance minimization varying the beam energy and the areal density of the foils with 20% increase and decrease systematically, and estimate the reduced χ^2 (equation A.4) over compartment 3,6 and 9. Variance minimization (Andrew's Niobium and iron paper + <https://sci-hub.tw/><https://doi.org/10.1016/j.nimb.2016.09.018>).

For compartment 3 ($E_d=25$ MeV) all seven monitor reactions were above threshold, thus 6 degrees of freedom. However, early in the target stack, the scattering was low, and the χ^2 does not tell how well the energy bin assignment work further back in the stack. For compartment 6 ($E_d=18$ MeV), all the six possible monitor reactions (for nickel and copper) were above threshold, and it gave a good estimate of how the beam current was developing throughout the stack. In compartment 9 ($E_d=10$ MeV), five monitor reactions are above threshold (except for ^{62}Zn). At the very end it is possible to see the full effect of the scattering.

With the assumption that the beamcurrent loss is zero over one compartment, a linear fit-model (using the scipy optimize curvefit function) with a slope equal to zero was used to estimate the beam current in each compartment, and with the estimated χ^2 .

Figure 5.10 shows the uncertainty weighted linear fit over compartment 6.

Table 5.1: The weighted average beam current before and after variance minimization in each compartment. The beam current on the 88-Inch Cyclotron beam integrator was 128.5 nA.

Compartment	Before	After
01	131.56 \pm 3.64	134.08 \pm 3.70
02	132.23 \pm 3.74	136.42 \pm 3.83
03	133.81 \pm 3.64	138.02 \pm 3.75
04	134.89 \pm 4.21	138.88 \pm 4.31
05	136.85 \pm 4.21	139.67 \pm 4.29
06	137.40 \pm 4.53	138.85 \pm 4.58
07	139.55 \pm 4.37	139.77 \pm 4.37
08	133.60 \pm 4.27	134.96 \pm 4.32
09	133.16 \pm 5.04	143.59 \pm 5.67
10	108.49 \pm 5.80	121.75 \pm 6.65

Figure 5.11 shows the beam current before and after variance minimization, and the weighted average beam currents are listed in table 5.2 estimated before and after the variance minimization. After variance minimization, the beam current estimated in each compartment (stabled lines) were similar, and meanwhile the weighted χ^2 was about the same in compartment 6, it has improved in compartment 3 and very visible in compartment 9. In general the points are also more aligned.

5.4 Cross sections

The cross sections were finally calculated via equation 3.18 as a function of the weighted average beam energy, the end of beamactivites for the product, the number of target nuclei, the weighted average beam current, the irradiation time and the decay constant of product. The cross section results are represented in the next chapter. Nuclei with beta and isomer feeding were reported as cumulative, as well as the first observed element in a decay chain was reported as cumulative, due to the possible feeding from short-lived activities. The remaining activities which were not subject to feeding were reported as independent.

The measured data is compared to previous experimental data from EXFOR, along with nuclear reactor models TALYS-1.9, TENDL-2019, ALICE-2017

Here write a few sentences about how each was done and the motivation behind it.

5.5 Estimation of the beam current

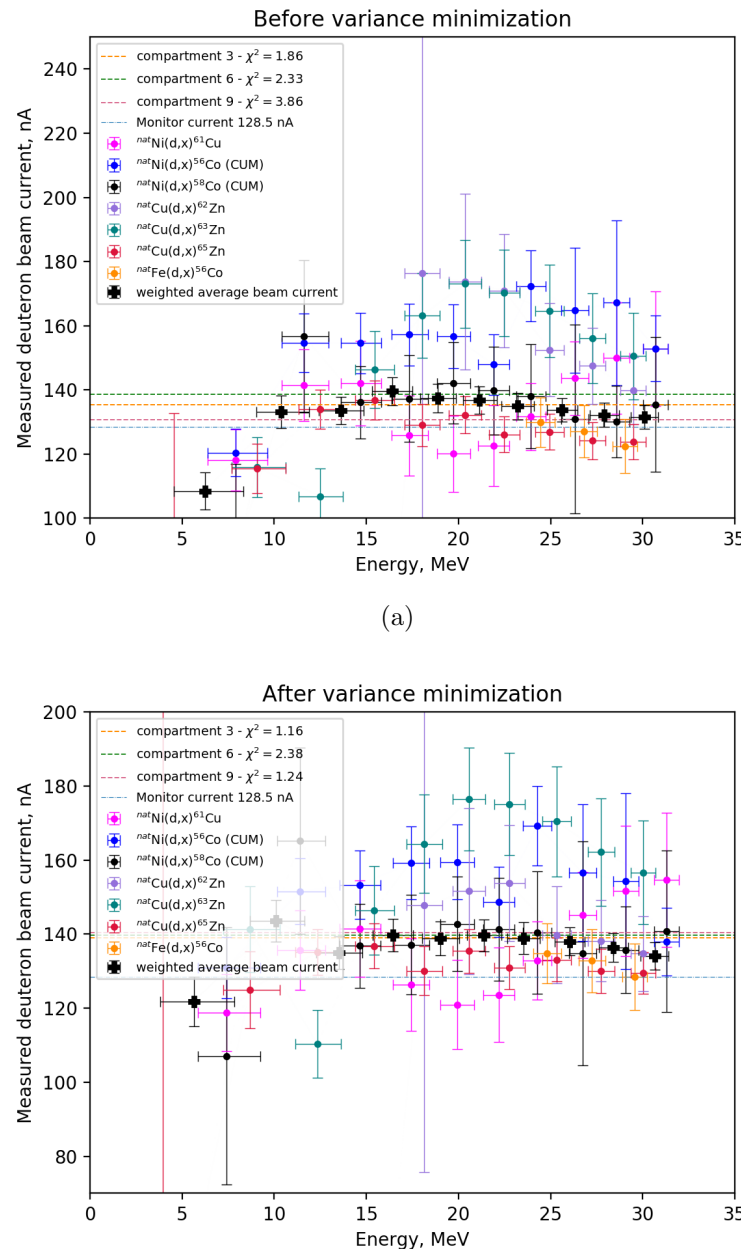
The beamintegrator measured a current of 128.5 nA in front of the beam stack. However in order to have precise cross section measurements, the nominal beam current in each foil was calculated. The IAEA recommended monitor reactions (2017) $^{nat}\text{Ni}(\text{d},\text{x})^{61}\text{Cu}$, ^{56}Fe , ^{58}Co , $^{nat}\text{Cu}(\text{d},\text{x})^{62,63,65}\text{Zn}$ and $^{nat}\text{Fe}(\text{d},\text{x})^{56}\text{Co}$

$$\Phi(E) = \frac{A_0}{N_T \sigma(E)_{\text{mon}} (1 - e^{-\lambda \Delta t_{\text{irr}}})} \quad (5.10)$$

Equation 5.10 builds upon the thin target assumption, which implies that the energy degradation in the foil is zero. However, we know that there is an energy distribution, which was estimated using NPAT's (Nuclear Physics Analysis Tool) Ziegler simulation³. The ziegler code simulates the deuteron transport based upon the Anderson & Ziegler stoppingpower formalism. Bethe-Block

Anderson & Ziegler is an empirical stopping power formalism, does not have any physics derivation behind it, and is a tuned model which reproduces experimental data. Bethe-Block is derived from basic E&M with no tuned parameters. Bethe-Block also gives the purely electronic stopping power,

³John's code, must cite.



(b) A 2% increase in beam current and a 4.25% increase in areal density gave the overall most consistent beam current, with reasonable values for the weighted .

Figure 5.8: Beam current before and after variance minimization.

the stopping power from an ion's interaction with the electronic cloud of an atom in the stopping medium. However the total stopping power is the sum of electronic, nuclear (elastic and inelastic scattering) and radiative stopping power, which is what we actually want from the experimental standpoint. Bethe-Block ignores nuclear and radiative.

, using Monte Carlo simulations [write a few sentences in theory...](#). The code provides the full deuteron energy and flux degradation in each foil, $d\phi/dE$, which can be visualized for the iridium foils in figure 5.9. Can be seen that as the deuteron energy is degraded, the mean value is shifted towards the low energy side, and the peak width increases. As stopping power is inversely proportional to the charge particle energy ($-\frac{dE}{dx} \propto \frac{1}{\beta^2}$, bethe block), and along with scattering taking place towards the end of stack, the low energy tail is more degraded, and we see a skew towards the low energy, creating a broader energy-flux profile and a shift of the mean value (centroid). This shift leads to an increasing uncertainty in energy. The (normalized) flux-weighted average energy for each foil was calculated, [ironpaper: which takes into account the slowing down of deuterons, and reports effective energy centroid of each foil](#), using the energy distributions $d\phi/dE$ provided by the Ziegler code:

$$\langle E \rangle = \frac{\int E \frac{d\phi}{dE} dE}{\int \frac{d\phi}{dE} dE} \quad (5.11)$$

The uncertainty in beam energy is divided into low energy and high energy tale, with the FWHM split by the centroid (figure 5.9).

Likewise, the energydependent monitor IAEA cross sections need to be flux-weighted over each foil. In order to do this, a spline interpolation over the energy array over each foil provided by the Ziegler simulation was spline interpolated with the IAEA recommended cross section data. Thus, the monitor cross section in equation 5.10 is modified to

$$\sigma(\langle E \rangle) = \frac{\int \sigma_{\text{mon}} \frac{d\phi}{dE} dE}{\int \frac{d\phi}{dE} dE} \quad (5.12)$$

With the end of beam activities for the monitor reactions, number of target nuclei and the flux-weighted IAEA cross sections, the beam current as a function of the flux-weighted average beam energy was estimated for each reaction in each foil.

5.5.1 Variance minimization of the deuteron transport calculations

In theory, the estimated beam current of a charge particle beam should be constant, until completely stopped, since the majority of the incident particles does not interact in nuclear reactions, but only lose energy via elastic and inelastic scattering. However, non-consistant values of the beam current, especially in the back of the stack can be due to energy bins being assigned wrongly in the energy distribution simulation done in Ziegler or a systematic error in the areal density which gets progressively worse further back in the stack (Niobium paper, Andrew). A way to work around these errors was to perform a variance minimization varying the beam energy and the areal density of the foils with 20% increase and decrease systematically, and estimate the reduced χ^2 (equation A.4) over compartment 3,6 and 9. Variance minimization (Andrew's Niobium and iron paper + <https://sci-hub.tw/><https://doi.org/10.1016/j.nimb.2016.09.018>).

For compartment 3 ($E_d=25$ MeV) all seven monitor reactions were above threshold, thus 6 degrees of freedom. However, early in the target stack, the scattering was low, and the χ^2 does not tell how well the energy bin assignment work further back in the stack. For compartment 6 ($E_d=18$ MeV), all the six possible monitor reactions (for nickel and copper) were above threshold, and it gave a good estimate of how the beam current was developing throughout the stack. In compartment 9 ($E_d=10$ MeV), five monitor reactions are above threshold (except for ^{62}Zn). At the very end it is possible to see the full effect of the scattering.

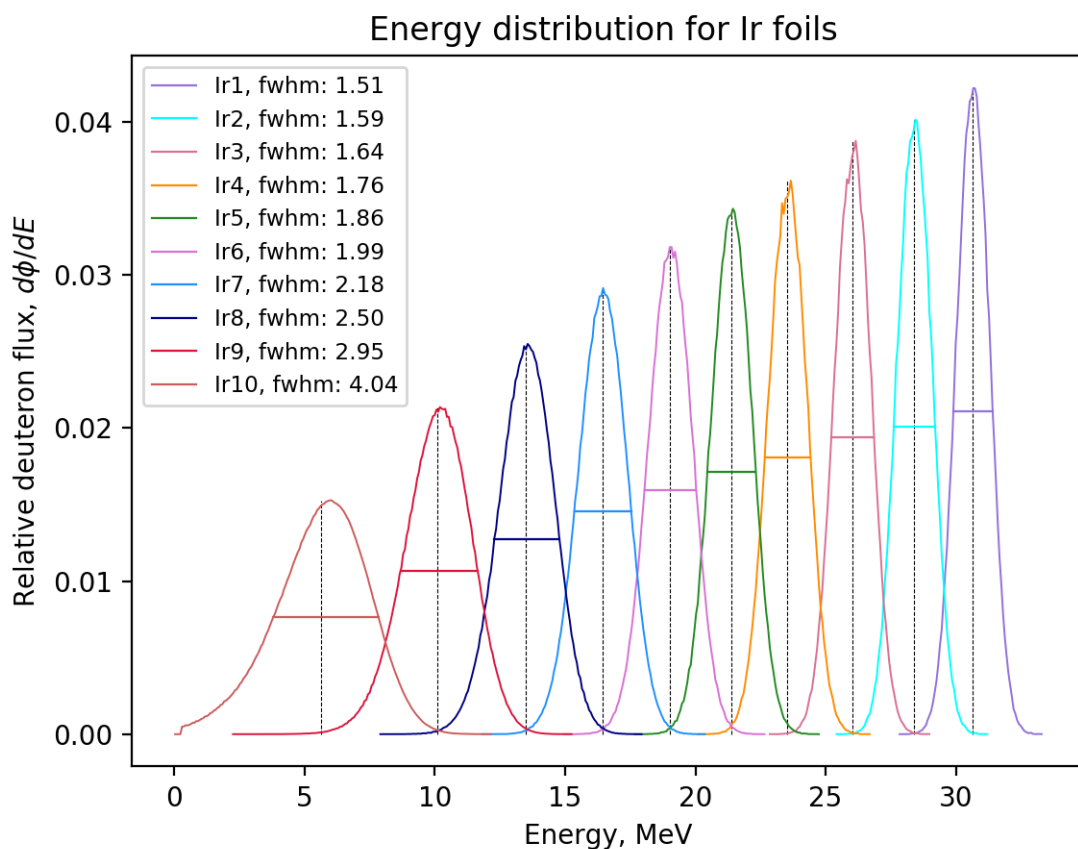


Figure 5.9: Iridium energy flux distribution over the 10 foils. As the energy degrades, skewed and larger full width half max. The vertical line in each peak is the mean value. This indicates that at lower energies, the right uncertainty is greater than the left uncertainty in the peak.

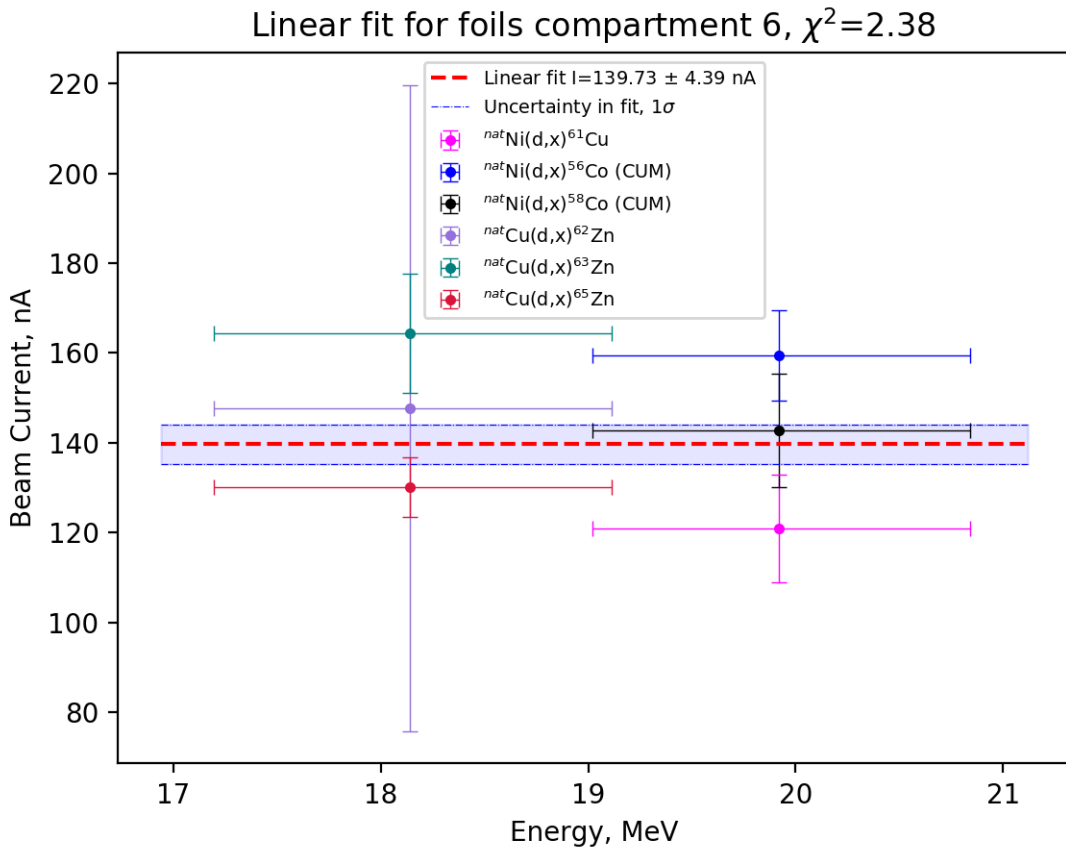


Figure 5.10: The estimated (uncertainty weighted) beamcurrent over compartment 6.

With the assumption that the beamcurrent loss is zero over one compartment, a linear fit-model (using the scipy optimize curvefit function) with a slope equal to zero was used to estimate the beam current in each compartment, and with the estimated χ^2 .

Figure 5.10 shows the uncertainty weighted linear fit over compartment 6.

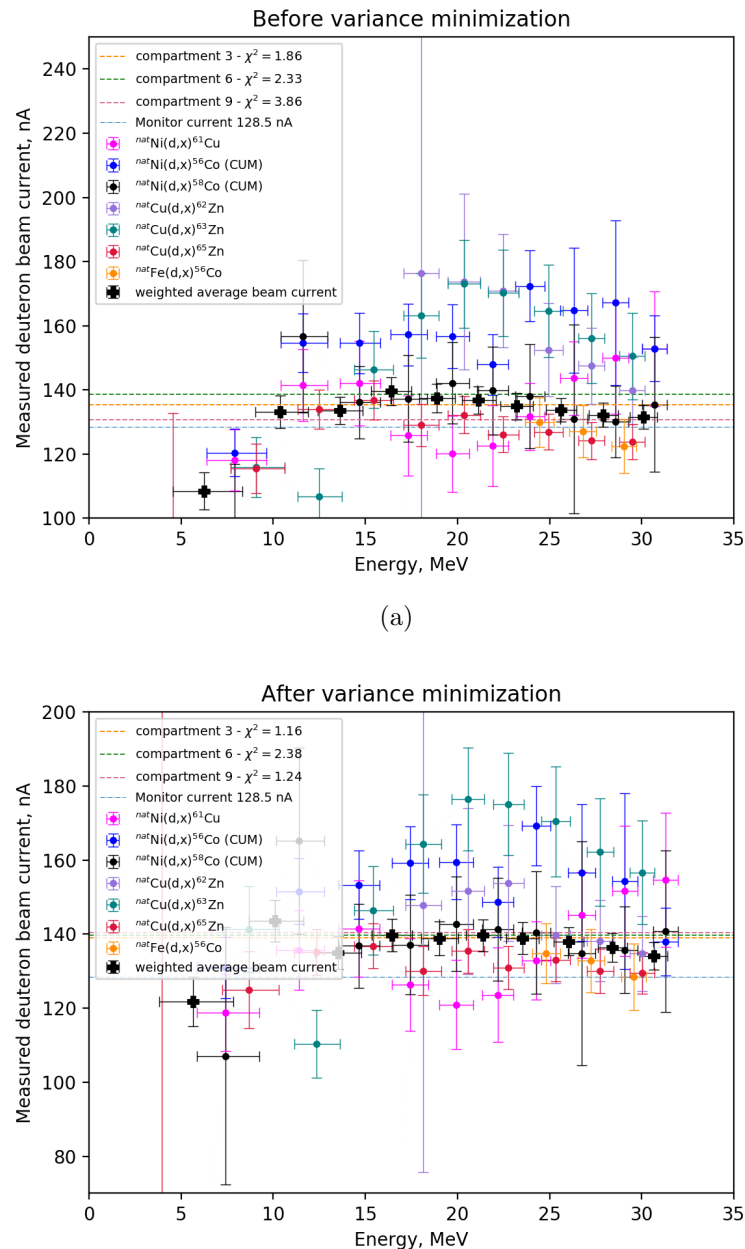
Figure 5.11 shows the beam current before and after variance minimization, and the weighted average beam currents are listed in table 5.2 estimated before and after the variance minimization. After variance minimization, the beam current estimated in each compartment (stabled lines) were similar, and meanwhile the weighted χ^2 was about the same in compartment 6, it has improved in compartment 3 and very visible in compartment 9. In general the points are also more aligned.

For cross section calculations, equation ?? is used, with the estimated weighted average beam current. Figure 5.12 shows the estimated cross sections for the monitor reactions, using the weighted average beam current over all monitor foils. The recommended monitor cross section data for the monitor reactions are also plotted, which was used in the cross section calculation.

5.6 Cross section measurements

With all variables for cross sections, cross sections can be calculated using equation ???. Since the energy was a flux-weighted average beam energy, the value that is provided as cross section is a flux-averaged cross section. An accurate measure of the cross section as a function of deuteron energy was possible, as the thin foils provides smaller average beam energy intervals, and it makes it possible to have more measurements if thick foils are replaced with several thinner (one single foil represents a single measurement). **in theory: Thin foils also produce minimal amounts of radioactivity, thus the deadtime of the detector and the dose to humans is low.**

Thin foils decreases the energy width, making a more precise measurement dependent on energy.



(b) A 2% increase in beam current and a 4.25% increase in areal density gave the overall most consistent beam current, with reasonable values for the weighted .

Figure 5.11: Beam current before and after variance minimization.

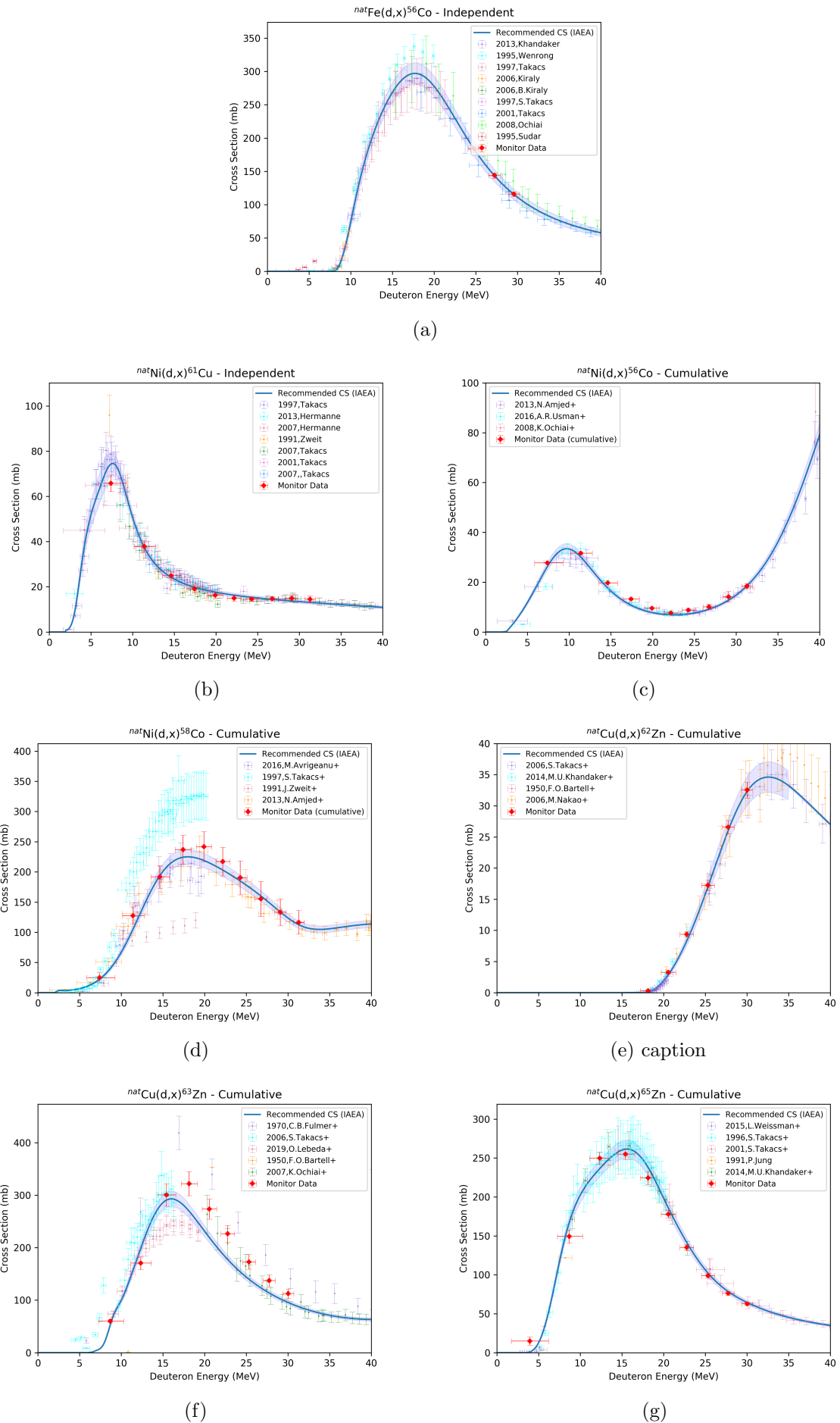


Figure 5.12: Figure shows the estimation of monitor cross section using the estimated weighted average beam current for each reaction (not the total). It is compared along with the recommended (IAEA) monitor data, and other experimental data

Table 5.2: The weighted average beam current before and after variance minimization in each compartment. The beam current on the 88-Inch Cyclotron beam integrator was 128.5 nA.

Compartment	Before	After
01	131.56 ±3.64	134.08 ±3.70
02	132.23 ±3.74	136.42 ±3.83
03	133.81 ±3.64	138.02 ±3.75
04	134.89 ±4.21	138.88 ±4.31
05	136.85 ±4.21	139.67 ±4.29
06	137.40 ±4.53	138.85 ±4.58
07	139.55 ±4.37	139.77 ±4.37
08	133.60 ±4.27	134.96 ±4.32
09	133.16 ±5.04	143.59 ±5.67
10	108.49 ±5.80	121.75 ±6.65

However the reported cross sections are flux-averaged over the energy distribution subtended by each foil.

The cross sections are reported as independent if there is nothing decaying into it (beta feeding or from isomer transition), which means that the first observed element in a decay chain is reported as cumulative unless it is the first possible element (which are the nuclei with one more proton more than the target nuclei, which for this experiment is Platinum (from Ir), Zink (from Cu), Copper (from Ni) and Cobalt (from Fe). If there is feeding, and the half life is much shorter or much longer than the specific nuclei, can choose appropriate timewindow and report as independent, when we know that the feeding has either died out or is very low!

If possible with feeding: added together to get cumulative or subtracted giving independent. Multiplying by branching ratio.

The measured cross sections in this work was compared to previous experimental data, along with reaction modelling codes TALYS^{https://sci-hub.tw/https://doi.org/10.1016/j.nds.2012.11.002}, TENDL, ALICE20 and CoH.

Optical model calculations performed first,

Talys takes in projectile, target element (specific isotope or all stable target isotopes), energy array with desired spacing and upper limit energy.

For COH: To get both 191Ir and 193Ir to run, we had to adjust the parameter "tweakSD", which adjusts the effective single-particle state density for a particular particle emission channel. In the end, we ran with tweakSD=0.25 for both outgoing alphas and neutrons (protons were unaffected). In other words, we set the single-particle state density for outgoing alphas and neutrons [(d,xa) and (d,xn) reactions] to be 25% of what they normally are, which is a HUGE change.

from talys cite p. 2843-2844: TENDL is developed from talys (TALYS evaluated Nuclear data Library). This library consists of a complete set of nuclear reaction data for incident neutrons, photons, protons, deuterons, tritons, Helium-3 and alpha particles, from 10^5 eV up to 200 MeV, for all 2430 isotopes from ^6Li to ^{281}Ds that are either stable or have a half-life longer than 1 second. All data are completely and consistently evaluated using a software system consisting of the TALYS nuclear reaction code, and other software to handle resonance data, experimental data, data from existing evaluations, and to provide the final ENDF-6 formatting, including covariance information. The result is a nuclear data library with mutually consistent reaction information for all isotopes and a quality that increases with yearly updates. To produce this library, TALYS input parameters are adjusted for many nuclides so that calculated cross sections agree with experimental data, while for important nuclides experimental or evaluated data are directly included. Also feedback from integral measurements is processed into the data libraries. For nuclides for which (almost) no experimental data exists, default TALYS calculations based on global models and parameters are used.

Dont understand this part.....

Appendix A

Statistics

Uncertainty in statistics refers to the standard deviation of the data, which gives a number of the spreading of the data from the mean value of the data citation. The variance is the standard deviation squared, which weights the variables to a higher degree.

$$std = \sqrt{\sigma^2} \quad (\text{A.1})$$

$$\sigma = \sqrt{\frac{1}{N} \sum_{i=1}^N (x_i - \bar{x})^2} \quad (\text{A.2})$$

where N is the number of measurements, x_i is a measurement and \bar{x} is the average over all measurements.

χ^2 is an estimation of the goodness of the fit, which includes the weight of the error

$$\chi^2 = \sum_i^n \left(\frac{y_i - \bar{y}}{\sigma_i} \right)^2 \quad (\text{A.3})$$

where \bar{y} is the mean value of y and σ_i is the error in y_i . The reduced χ^2 is defined as the χ^2 per degree of freedom

$$\chi_\nu^2 = \frac{\chi^2}{\nu} \quad (\text{A.4})$$

where ν is the degrees of freedom equal to the number of observations minus the number of fitted parameters. A value close to $\chi_\nu^2 = 1$ indicates that the observations and fit is in well accordance to the error, while $\chi_\nu^2 > 1$ indicates an underfitting and a $\chi_\nu^2 < 1$ indicates an overfitting¹.

A function f with input x and a set of variables $\vec{\beta} = \beta_1, \beta_2, \dots, \beta_n$ and output y can be written on the following form

$$y = f(x, \vec{\beta}) \quad (\text{A.5})$$

The uncertainty in y is dependent on the uncertainty in the different input variables $\vec{\beta}$. The matrix expression for error propagation is (Tellinghuisen, Joel, Statistical error propagation)²

$$\sigma_y^2 = \mathbf{J} \cdot \mathbf{V} \cdot \mathbf{J}^T \quad (\text{A.6})$$

where σ_y^2 is the variance in y, J is the Jacobian matrix

$$\mathbf{J} = \begin{bmatrix} \frac{\partial f}{\partial \beta_1} & \frac{\partial f}{\partial \beta_2} & \dots & \frac{\partial f}{\partial \beta_n} \end{bmatrix} \quad (\text{A.7})$$

and V is the variance-covariance matrix

¹https://en.wikipedia.org/wiki/Reduced_chi-squared_statistic

²A full derivation of the expression can be found in Uncertainty Propagation for Measurements with multiple output quantities, Dobbert, Schrijver

$$\mathbf{V} = \begin{bmatrix} \sigma_0^2 & \sigma_{0,1} & \cdots & \sigma_{0,n} \\ \sigma_{1,0} & \sigma_1^2 & \cdots & \sigma_{1,n} \\ \vdots & \vdots & \ddots & \vdots \\ \sigma_{n,0} & \sigma_{n,1} & \cdots & \sigma_n^2 \end{bmatrix} \quad (\text{A.8})$$

In the cases where the input parameters are uncorrelated, all non-diagonal elements in the variance-covariance matrix is equal to zero, and the expression for the variance is simplified to

$$\sigma_y^2 = \sum_{i=1}^n \left(\frac{\partial f}{\partial \beta_i} \right)^2 \sigma_{\beta_i}^2 \quad (\text{A.9})$$

Whenever the input parameters are correlated, which means that $\sigma_{\beta_i, \beta_j} \neq 0$, we have to apply equation A.6, otherwise, the simplification in equation A.9 will give wrong error propagation.

To evaluate the partial derivatives of f , the computational derivation is applicable

$$\frac{\partial f}{\partial \beta_i} \approx \frac{f(x, \beta_i + \frac{\Delta \beta_i}{2}) - f(x, \beta_i - \frac{\Delta \beta_i}{2})}{\Delta \beta_i} \quad (\text{A.10})$$

where $\Delta \beta_i$ is a small number, like $10^{-8} \beta_i$.

For a function $f = xy$, the variance can be expressed from equation A.6, where

$$\mathbf{J} = [y \quad x]$$

and

$$\mathbf{V} = \begin{bmatrix} \sigma_x^2 & \sigma_{x,y} \\ \sigma_{y,x} & \sigma_y^2 \end{bmatrix}$$

$$\sigma_f^2 = x^2 \sigma_y^2 + y^2 \sigma_x^2 + 2xy \sigma_{x,y} \quad (\text{A.11})$$

If we multiply each term so that we can collect f^2 in the numerator, the variance in f can be expressed as

$$\sigma_f^2 = f^2 \left(\frac{\sigma_x^2}{x^2} + \frac{\sigma_y^2}{y^2} + \frac{2\sigma_{x,y}}{xy} \right) \quad (\text{A.12})$$

if the variables x and y are uncorrelated, the variance is further simplified, and more terms can be included easily. The simplified standard deviation of a function $f(\bar{\beta}) = \beta_1 \cdot \beta_2 \cdots \beta_n$ with uncorrelated variables is thus

$$\sigma_f = |f| \sqrt{\left(\frac{\sigma_{\beta_1}}{\beta_1} \right)^2 + \left(\frac{\sigma_{\beta_2}}{\beta_2} \right)^2 + \cdots + \left(\frac{\sigma_{\beta_n}}{\beta_n} \right)^2} \quad (\text{A.13})$$

Appendix B

Tables

For all tables, the assumption is that the main particle emission is due to alpha, proton or neutron emission. However, triton, ^3He and deuterons are still fed when above threshold, but from theory, the feeding is low. For triton, ^3He and deuteron respectively, subtract 8.5, 7.7 or 2.2 respectively from the Q value. Alphaparticles (due to the large binding energy and spin equal to 0) will be more fed. To calculate Q value for alpha emission subtract 28.3 MeV from Q value of 2p2n-reactions. Q values from ¹ are used. Q values below 40 MeV are included for comparison to experimental data.

B.1 Product nuclei, Q-values and gammarays

Table B.1: Products observed on Nickel foils. Nickel has five stable isotopes: ^{58}Ni (68.077%), ^{60}Ni (26.223 %), ^{61}Ni (1.1399%), ^{62}Ni (3.6346%) and ^{64}Ni (0.9255%). If the nucleus has provided energy level, the nucleus is an isomer, if nothing then ground state. **The table is inspired by Tarkanyi et al 2019 (ir paper)**

Nuclide level (keV)	Half life	Decay mode	Reaction route	Q value (keV)	E_{γ} (keV)	I_{γ} (%)
^{52}Mn (0.0)	5.591 d 21.1 m	ϵ : 100%	$^{58}\text{Ni}(\text{d},2\alpha)$	-1235.6	744.233	90.0
			$^{60}\text{Ni}(\text{d},2\text{n}2\alpha)$	-21622.6	935.544	94.5
			$^{61}\text{Ni}(\text{d},3\text{n}2\alpha)$	-29442.7	1246.278	4.21
					1434.092	100.0
^{54}Mn (0.0)	312.20 d	ϵ : 100%	$^{58}\text{Ni}(\text{d},2\text{p}\alpha)$	-8538.3	834.848	99.9760
			$^{60}\text{Ni}(\text{d},2\alpha)$	-629.6		
			$^{61}\text{Ni}(\text{d},\text{n}2\alpha)$	-8449.7		
			$^{62}\text{Ni}(\text{d},2\text{n}2\alpha)$	-19045.4		
^{59}Fe (0.0)	44.490 d	β^- : 100%	$^{60}\text{Ni}(\text{d},3\text{p})$	-12539.5	1291.590	43.2
			$^{61}\text{Ni}(\text{d},\text{n}3\text{p})$	-20359.6		
			$^{62}\text{Ni}(\text{d},\text{p}\alpha)$	-2659.7		
			$^{64}\text{Ni}(\text{d},2\text{n}\text{p}\alpha)$	-19154.9		
^{55}Co (0.0)	17.53 h	ϵ : 100%	$^{58}\text{Ni}(\text{d},\text{n}\alpha)$	-3559.4	385.4	0.54
			$^{60}\text{Ni}(\text{d},3\text{n}\alpha)$	-23946.4	520.0	0.83
			$^{61}\text{Ni}(\text{d},4\text{n}\alpha)$	-31766.5	803.7	1.87
					931.1	75
					1212.8	0.26
					1316.6	7.1
					1370.0	2.9
					2177.6	0.29

¹<https://www.nndc.bnl.gov/qcalc/>

APPENDIX B. TABLES

^{56}Co (0.0)	77.236 d	$\epsilon : 100\%$	$^{58}\text{Ni}(\text{d},\alpha)$ $^{61}\text{Ni}(\text{d},2\text{n}\alpha)$ $^{61}\text{Ni}(\text{d},3\text{n}\alpha)$ $^{62}\text{Ni}(\text{d},4\text{n}\alpha)$	6522.5 -13864.5 -21684.6 -32280.4	787.743 846.770 977.372 1175.101 1963.741 2015.215 2034.791	0.3111 99.9399 1.421 2.252 0.707 3.016 7.77
^{57}Co (0.0)	271.74 d	$\epsilon : 100\%$	$^{58}\text{Ni}(\text{d},\text{n}2\text{p})$ $^{60}\text{Ni}(\text{d},\text{n}\alpha)$ $^{61}\text{Ni}(\text{d},2\text{n}\alpha)$ $^{62}\text{Ni}(\text{d},3\text{n}\alpha)$	-10396.7 -2488.1 -10308.2 -20903.9	122.06065 136.47365	85.60 10.68
^{58}Co (0.0)	70.86 d	$\epsilon : 100\%$	$^{58}\text{Ni}(\text{d},2\text{n})$ $^{60}\text{Ni}(\text{d},\alpha)$ $^{61}\text{Ni}(\text{d},\text{n}\alpha)$ $^{62}\text{Ni}(\text{d},2\text{n}\alpha)$ $^{64}\text{Ni}(\text{d},4\text{n}\alpha)$	-1823.8 6084.9 -1735.3 -12331.0 -28826.2	810.7593 863.951 1674.725	99.450 0.686 0.517
^{58m}Co (24.88921)	9.10 h	IT:100%	$^{58}\text{Ni}(\text{d},2\text{n})$ $^{60}\text{Ni}(\text{d},\alpha)$ $^{61}\text{Ni}(\text{d},\text{n}\alpha)$ $^{62}\text{Ni}(\text{d},2\text{n}\alpha)$ $^{64}\text{Ni}(\text{d},4\text{n}\alpha)$	-1848.7 6060.0 -1760.2 -12355.9 -28851.1	-	-
^{60}Co (0.0)	1925.28 d	$\beta^- : 100\%$	$^{60}\text{Ni}(\text{d},2\text{p})$ $^{61}\text{Ni}(\text{d},\text{n}2\text{p})$ $^{62}\text{Ni}(\text{d},\alpha)$ $^{64}\text{Ni}(\text{d},2\text{n}\alpha)$	-4265.0 -12085.1 5614.8 -10880.4	1173.228 1332.492	99.85 99.9826
^{56}Ni (0.0)	6.075 d	$\epsilon : 100\%$	$^{58}\text{Ni}(\text{d},3\text{np})$	-24688.4	158.38 480.44 749.95 811.85 1561.80	98.8 36.5 49.5 86.0 14.0
^{57}Ni (0.0)	35.60 h	$\beta^+ : 100\%$	$^{58}\text{Ni}(\text{d},2\text{np})$ $^{60}\text{Ni}(\text{d},4\text{np})$	-14440.8 -34827.8	1757.55 1919.52 2804.20	5.75 12.3 0.098
^{65}Ni (0.0)	2.51719 h	$\beta^- : 100\%$	$^{64}\text{Ni}(\text{d},\text{p})$	3873.51	366.27 1481.84 1623.42 1724.92	4.81 23.59 0.498 0.399
^{60}Cu (0.0)	23.7 m	$\epsilon : 100\%$	$^{60}\text{Ni}(\text{d},2\text{n})$ $^{61}\text{Ni}(2,3\text{n})$ $^{62}\text{Ni}(\text{d},4\text{n})$	-9134.9 -16955.0 -27550.7	467.3 497.9 643.2 952.4 1035.2 1110.5 1293.7 1791.6 1861.6 1936.9 2061.0 2158.9 2403.3 2687.9 2746.1	3.52 1.67 0.97 2.73 3.70 1.06 1.85 45.4 4.8 2.20 0.79 3.34 0.77 0.44 1.06

B.1. PRODUCT NUCLEI, Q-VALUES AND GAMMARAYS

^{61}Cu	3.339 h	$\epsilon : 100\%$	$^{60}\text{Ni}(\text{d},\text{n})$	2575.3	282.956	12.2
			$^{61}\text{Ni}(\text{d},2\text{n})$	-5244.8	373.050	2.1
			$^{62}\text{Ni}(\text{d},3\text{n})$	-15840.5	529.169	0.38
			$^{64}\text{Ni}(\text{d},5\text{n})$	-32335.7	588.605	1.17
					625.605	0.040
					656.008	10.8
					816.692	0.31
					841.211	0.21
					902.294	0.083
					1032.162	0.043
					1073.465	0.033
					1132.351	0.090
					1185.234	3.7
					1446.492	0.045
^{64}Cu	12.701 h	$\epsilon : 100\%$	$^{64}\text{Ni}(\text{d},2\text{n})$	-4681.3	1345.77	0.475
		$\beta^- : 38.5\%$				

APPENDIX B. TABLES

Table B.2: Products observed on Iron foils. Iron has five stable isotopes: ^{54}Fe (5.845%), ^{56}Fe (91.754 %), ^{57}Fe (2.119%) and ^{58}Fe (0.282%). If the nucleus has provided energy level, the nucleus is an isomer, if nothing then ground state. **The table is inspired by Tarkanyi et al 2019 (ir paper)**

Nuclide level (keV)	Half life	Decay mode	Reaction route	Q value (keV)	E_γ (keV)	I_γ (%)
^{48}V (0.0)	15.9735 d	$\epsilon : 100\%$	$^{54}\text{Fe}(\text{d},2\alpha)$	-3490.9	944.130	7.870
			$^{56}\text{Fe}(\text{d},2\text{n}2\alpha)$	-23986.1	983.525	99.98
			$^{57}\text{Fe}(\text{d},3\text{n}2\alpha)$		1312.106	98.2
^{51}Cr (0.0)	27.704 d	$\epsilon : 100\%$	$^{54}\text{Fe}(\text{d},\text{p}\alpha)$	-1381.3	320.0824	9.910
			$^{56}\text{Fe}(\text{d},2\text{n}\alpha)$	-21876.5		
			$^{57}\text{Fe}(\text{d},3\text{n}\alpha)$	-29522.6		
			$^{58}\text{Fe}(\text{d},4\text{n}\alpha)$	-39567.2		
^{52}Mn (0.0)	5.591 d d	$\epsilon : 100\%$	$^{54}\text{Fe}(\text{d},\alpha)$	5163.6	346.02	0.980
			$^{56}\text{Fe}(\text{d},2\text{n}\alpha)$	-15331.6	744.233	90.0
			$^{57}\text{Fe}(\text{d},3\text{n}\alpha)$	-22977.7	848.18	3.32
					935.544	94.5
					1246.278	4.21
					1333.649	5.07
					1434.092	100.0
^{54}Mn (0.0)	312.20 d	$\epsilon : 100\%$	$^{54}\text{Fe}(\text{d},2\text{p})$	-2139.1	834.8480	99.9760
			$^{56}\text{Fe}(\text{d},\alpha)$	5661.4		
			$^{57}\text{Fe}(\text{d},\text{n}\alpha)$	-1984.7		
			$^{58}\text{Fe}(\text{d},2\text{n}\alpha)$	-12029.3		
^{53}Fe (0.0)	8.51 m ????	$\epsilon : 100\%$	$^{54}\text{Fe}(\text{d},2\text{np})$	-15602.9	377.9	42%
			$^{56}\text{Fe}(\text{d},4\text{np})$	-36098.1		
^{59}Fe (0.0)	44.490 d	$\beta^- : 100\%$	$^{58}\text{Fe}(\text{d},\text{p})$	4356.44	1099.245	56.5
					1291.590	43.2
^{55}Co (0.0)	17.53 h	$\epsilon : 100\%$	$^{54}\text{Fe}(\text{d},\text{n})$	2839.8	91.9	1.16
			$^{56}\text{Fe}(\text{d},3\text{n})$	-17655.4	477.2	20.2
			$^{57}\text{Fe}(\text{d},4\text{n})$	-25301.5	803.7	1.87
					827.0	0.21
					931.1	75
					1316.6	7.1
					1370.0	2.9
					1408.5	16.9
					2177.6	0.29
					2872.4	0.118
					2938.9	0.057

^{56}Co (0.0)	77.236 d	$\epsilon : 100\%$	$^{56}\text{Fe}(\text{d},2\text{n})$ $^{57}\text{Fe}(\text{d},3\text{n})$ $^{58}\text{Fe}(\text{d},4\text{n})$	-7573 -15219.7 -25264.3	263.434 486.55 733.514 787.743 846.770 852.732 896.510 977.372 996.948 1037.843 1140.368 1159.944 1175.101 1198.888 1238.288 1335.40 1360.212 1771.357 1963.741 2015.215 2034.791 2212.944 2276.131 2598.500	0.0220 0.0540 0.191 0.311 99.9399 0.049 0.073 1.421 0.111 14.05 0.132 0.094 2.252 0.049 66.46 0.1224 4.283 15.41 0.707 3.016 7.77 0.388 0.118 16.97
^{57}Co (0.0)	271.74 d	$\epsilon : 100\%$	$^{56}\text{Fe}(\text{d},\text{n})$ $^{57}\text{Fe}(\text{d},2\text{n})$ $^{58}\text{Fe}(\text{d},3\text{n})$	3802.9 -3843.2 -13887.8	122.06065 136.47356	85.60 10.68
^{58}Co (0.0)	70.86	$\epsilon : 100\%$	$^{57}\text{Fe}(\text{d},\text{n})$ $^{58}\text{Fe}(\text{d},2\text{n})$	4729.7 -5314.9	810.7593	99.450

APPENDIX B. TABLES

Table B.3: Products observed on Copper foils. Copper has two stable isotopes: ^{63}Cu (69.15%) and ^{65}Cu (30.85 %). If the nucleus has provided energy level, the nucleus is an isomer, if nothing then ground state. **The table is inspired by Tarkanyi et al 2019 (ir paper))**

Nuclide level (keV)	Half life	Decay mode	Reaction route	Q value (keV)	E_{γ} (keV)	I_{γ} (%)
^{59}Fe (0.0)	44.490 d	β^- : 100%	$^{63}\text{Cu}(\text{d},2\text{p}\alpha)$	-8782.1	1099.245	56.5
			$^{65}\text{Cu}(\text{d},2\alpha)$	1687.0	1291.590	43.2
^{60}Co (0.0)	1925.28 d	β^- : 100%	$^{63}\text{Cu}(\text{d},\text{p}\alpha)$	-507.6	1173.228	99.85
			$^{65}\text{Cu}(\text{d},2\text{n}\alpha)$	-18334.1	1332.492	99.9826
^{61}Co (0.0)	1.649 h	β^- : 100%	$^{63}\text{Cu}(\text{d},\text{n}3\text{p})$	-19484.2	67.412	84.7
			$^{65}\text{Cu}(\text{d},\text{n}p\alpha)$	-9015.1		
^{65}Ni (0.0)	2.51719 h	β^- : 100%	$^{65}\text{Cu}(\text{d},2\text{p})$	-3580.2	1481.84	23.59
			$^{63}\text{Cu}(\text{d},3\text{np})$	-21962.9	282.956	12.2
^{61}Cu (0.0)	3.339 h	ϵ : 100%	$^{65}\text{Cu}(\text{d},5\text{np})$	-39789.4	656.008	10.8
					1185.234	3.7
^{64}Cu (0.0)	12.701 h	ϵ : 61.5% β^- : 38.5	$^{63}\text{Cu}(\text{d},\text{p})$	5691.54	1345.77	0.475
			$^{65}\text{Cu}(\text{d},2\text{np})$	-12135.0		
^{62}Zn (0.0)	9.193 h	ϵ : 100%	$^{63}\text{Zn}(\text{d},3\text{n})$	-15490.0	40.85	25.5
			$^{65}\text{Cu}(\text{d},5\text{n})$	-33316.6	243.36	2.52
					246.95	1.90
					260.43	1.35
					304.88	0.29
					394.03	2.24
					548.35	15.3
					596.56	26.0
					637.41	0.25
^{63}Zn (0.0)	38.47 m	ϵ : 100%	$^{63}\text{Cu}(\text{d},2\text{n})$	-6373.3	449.93	0.236
			$^{65}\text{Cu}(\text{d},4\text{n})$	-24199.8	669.62	8.2
					962.06	6.5
^{65}Zn (0.0)	243.93 d	ϵ : 100%	$^{65}\text{Cu}(\text{d},2\text{n})$	-4358.6	1115.539	50.04

Table B.4: Products observed in Iridium foils. Iridium has two stable isotopes: ^{191}Ir (37.3%) and ^{93}Ir (62.7 %). If the nucleus has provided energy level, the nucleus is an isomer, if nothing then ground state. **The table is inspired by Tarkanyi et al 2019 (ir paper)**

Nuclide level (keV)	Half life	Decay mode	Reaction route	Q value (keV)	E_{γ} (keV)	I_{γ} (%)
^{188}Ir (0.0)	41.5 h	ϵ : 100%	$^{191}\text{Ir}(\text{d},4\text{np})$	-24802.0	1209.80	6.9
					1715.67	6.2
					2059.65	7.0
^{189}Ir (0.0)	13.2 d	ϵ : 100%	$^{191}\text{Ir}(\text{d},4\text{np})$	-16626.0	95.23	0.38
					216.7	0.52
			$^{193}\text{Ir}(\text{d},5\text{np})$	-30596.0	233.5	0.30
					245.1	6.0
^{190}Ir (0.0)	11.78 d	ϵ : 100%	$^{191}\text{Ir}(\text{d},2\text{np})$	-10251.1	294.75	6.6
					380.03	2.03
			$^{193}\text{Ir}(\text{d},4\text{np})$	-24221.2	1036.05	2.42
$^{190m^2}\text{Ir}$ (376.4)	3.087 h	IT:8.6% ϵ : 91.4%	361.2	86.72
					502.5	89.38
					616.5	90.14
^{192}Ir (0.0)	73.829 d	ϵ : 4.76% β^- : 95.24%	$^{191}\text{Ir}(\text{d},\text{p})$	3973.55	201.3112	0.471
					295.95650	28.71
			$^{193}\text{Ir}(\text{d},2\text{np})$	-9996.6	374.4852	0.727
					416.4688	0.670
					468.06885	47.84
					489.06	0.438
					612.46215	5.34
					1061.49	0.0531
			$^{194}\text{Ir}(\text{d},\text{p})$	3842.22	293.541	2.5
					300.741	0.35
					589.179	0.140
					938.69	0.60
					1150.75	0.60
					1468.91	0.19
$^{194m^2}\text{Ir}$ (190+X)	171 d	β^- : 100%	338.8	55
					482.6	97
					562.4	35
					687.8	3.6
^{188}Pt (0.0)	10.16 d	ϵ : 99.999974% α : $2.6E - 5\%$	$^{191}\text{Pt}(\text{d},2\text{n})$	-26109.0	195.05	18.4
					381.43	7.4
^{189}Pt (0.0)	10.87 h	ϵ : 100%	$^{191}\text{Ir}(\text{d},4\text{n})$	-19389.0	94.34	6.5
					113.82	2.5
					243.50	5.9
					317.65	2.8
					721.38	7.9
^{191}Pt (0.0)	2.802 d	ϵ : 100%	$^{191}\text{Ir}(\text{d},2\text{n})$	-4017.0	178.96	12.5
					351.17	42.6
			$^{193}\text{Ir}(\text{d},4\text{n})$	-17988.0	409.44	100
					456.47	42
					538.87	181
					624.06	18.5
^{193m}Pt (149.783)	4.33 d	IT:100%	$^{193}\text{Ir}(\text{d},2\text{n})$	-3063.5	66.831	7.21
					135.5	0.1145475

Table B.5: Iridium production cross sections produced from Iridium

E_d (MeV)	Production cross section (mb) for iridium radionuclides				
	$^{188m1+g}\text{Ir}_{\text{cum}}$	$^{188m1+g}\text{Ir}_{\text{ind}}$	$^{189}\text{Ir}_{\text{cum}}$	$^{190m1+g}\text{Ir}_{\text{cum}}$	$^{190m1+g}\text{Ir}_{\text{ind}}$
$30.65^{+0.76}_{-0.75}$	1.37 ± 0.10	0.42 ± 0.03	332.49 ± 24.20	86.65 ± 2.89	85.88 ± 2.86
$28.40^{+0.80}_{-0.79}$	0.45 ± 0.07	0.17 ± 0.02	237.84 ± 17.44	62.80 ± 2.14	62.36 ± 2.13
$26.03^{+0.82}_{-0.82}$	0.34 ± 0.08	0.17 ± 0.03	91.49 ± 5.47	44.26 ± 1.47	44.01 ± 1.46
$23.54^{+0.88}_{-0.87}$	-	-	19.23 ± 2.65	27.29 ± 1.02	27.19 ± 1.02
$21.38^{+0.94}_{-0.92}$	-	-	-	18.73 ± 0.71	18.69 ± 0.70
$19.03^{+1.00}_{-0.99}$	-	-	-	14.02 ± 0.55	14.00 ± 0.55
$16.43^{+1.11}_{-1.08}$	-	-	-	12.40 ± 0.51	12.39 ± 0.51
$13.51^{+1.28}_{-1.22}$	-	-	-	8.26 ± 0.43	8.25 ± 0.42
$10.09^{+1.55}_{-1.41}$	-	-	-	-	-
$5.63^{+2.21}_{-1.83}$	-	-	-	-	-

Table B.6: Iridium production cross sections produced from Iridium

E_d (MeV)	Production cross section (mb) for iridium radionuclides			
	$^{190m2}\text{Ir}_{\text{ind}}$	$^{192}\text{Ir}_{\text{cum}}$	$^{194g}\text{Ir}_{\text{cum}}$	$^{194m2}\text{Ir}_{\text{ind}}$
$30.65^{+0.76}_{-0.75}$	8.87 ± 0.25	188.43 ± 5.27	50.92 ± 2.18	-
$28.40^{+0.80}_{-0.79}$	5.03 ± 0.15	152.55 ± 4.39	51.39 ± 2.89	-
$26.03^{+0.82}_{-0.82}$	2.92 ± 0.08	124.33 ± 3.42	61.37 ± 2.39	0.74 ± 0.17
$23.54^{+0.88}_{-0.87}$	1.16 ± 0.04	100.03 ± 3.14	69.68 ± 2.76	0.68 ± 0.26
$21.38^{+0.94}_{-0.92}$	0.45 ± 0.01	90.41 ± 2.80	86.38 ± 3.18	0.65 ± 0.13
$19.03^{+1.00}_{-0.99}$	0.16 ± 0.01	90.65 ± 3.01	97.79 ± 3.99	0.60 ± 0.14
$16.43^{+1.11}_{-1.08}$	0.06 0.00	99.61 ± 3.14	121.54 ± 4.54	0.50 ± 0.09
$13.51^{+1.28}_{-1.22}$	0.03 0.00	107.41 ± 3.48	143.27 ± 5.52	-
$10.09^{+1.55}_{-1.41}$	0.02 0.00	64.27 ± 2.56	92.78 ± 4.21	-
$5.63^{+2.21}_{-1.83}$	0.02 0.00	6.67 ± 0.37	6.32 ± 0.42	-

B.2 Production cross sections

B.2.1 ${}^{\text{nat}}\text{Ir}(\text{d},\text{x})$

Table B.7: Platinum production cross sections produced from Iridium

E_d (MeV)	Production cross section (mb) for platinum radionuclides			
	$^{188}\text{Pt}_{\text{ind}}$	$^{189}\text{Pt}_{\text{ind}}$	$^{191}\text{Pt}_{\text{ind}}$	$^{193m}\text{Pt}_{\text{ind}}$
$30.65^{+0.76}_{-0.75}$	0.94 ± 0.13	486.47 ± 21.86	597.10 ± 16.55	48.11 ± 6.33
$28.40^{+0.80}_{-0.79}$	0.30 ± 0.09	341.24 ± 16.64	483.60 ± 13.79	46.78 ± 2.19
$26.03^{+0.82}_{-0.82}$	0.17 ± 0.05	172.11 ± 8.03	353.99 ± 9.67	55.68 ± 2.17
$23.54^{+0.88}_{-0.87}$	-	30.72 ± 1.48	165.12 ± 5.15	51.79 ± 2.12
$21.38^{+0.94}_{-0.92}$	-	1.04 ± 0.07	71.05 ± 2.19	58.31 ± 1.96
$19.03^{+1.00}_{-0.99}$	-	0.09 ± 0.02	77.53 ± 2.57	77.98 ± 2.89
$16.43^{+1.11}_{-1.08}$	-	-	128.24 ± 4.03	115.33 ± 4.09
$13.51^{+1.28}_{-1.22}$	-	-	137.37 ± 4.42	148.98 ± 5.54
$10.09^{+1.55}_{-1.41}$	-	-	53.45 ± 2.12	56.18 ± 2.85
$5.63^{+2.21}_{-1.83}$	-	-	1.05 ± 0.06	1.56 ± 0.12

Table B.8:

E_d (MeV)	Production cross section (mb) for ...				
	$^{48}\text{V}_{\text{cum}}$	$^{51}\text{Cr}_{\text{cum}}$	$^{52}\text{Mn}_{\text{cum}}$	$^{54}\text{Mn}_{\text{ind}}$	$^{53}\text{Fe}_{\text{cum}}$
$29.57^{+0.68}_{-0.68}$	0.12 ± 0.01	7.54 ± 0.23	16.00 ± 0.36	23.85 ± 0.70	5.12 ± 0.65
$27.26^{+0.73}_{-0.72}$	0.09 ± 0.01	7.86 ± 0.25	5.48 ± 0.16	24.18 ± 0.72	2.77 ± 0.44
$24.80^{+0.77}_{-0.76}$	0.06 ± 0.00	8.51 ± 0.29	0.91 ± 0.03	26.12 ± 0.79	1.29 ± 0.30

Table B.9:

E_d (MeV)	Production cross section (mb) for ...			
	$^{59}\text{Fe}_{\text{ind}}$	$^{55}\text{Co}_{\text{ind}}$	$^{57}\text{Co}_{\text{ind}}$	$^{58}\text{Co}_{\text{ind}}$
0.16 ± 0.02	27.15 ± 0.80	35.91 ± 1.06	1.50 ± 0.05	$29.57^{+0.68}_{-0.68}$
$27.26^{+0.73}_{-0.72}$	0.15 ± 0.02	20.44 ± 0.60	38.37 ± 1.13	1.62 ± 0.05
$24.80^{+0.77}_{-0.76}$	0.18 ± 0.04	13.82 ± 0.40	42.63 ± 1.27	2.05 ± 0.07

Table B.10:

E_d (MeV)	Production cross section (mb) for ...					
	$^{59}\text{Fe}_{\text{cum}}$	$^{60}\text{Co}_{\text{cum}}$	$^{61}\text{Co}_{\text{cum}}$	$^{65}\text{Ni}_{\text{ind}}$	$^{61}\text{Cu}_{\text{cum}}$	$^{64}\text{Cu}_{\text{ind}}$
$30.03^{+0.67}_{-0.67}$	0.21 ± 0.03	9.49 ± 0.52	1.62 ± 0.09	3.42 ± 1.76	4.54 ± 0.87	170.76 ± 7.76
$27.74^{+0.72}_{-0.71}$	0.18 ± 0.02	11.38 ± 0.51	0.82 ± 0.07	3.84 ± 1.94	2.07 ± 0.95	153.78 ± 8.20
$25.32^{+0.77}_{-0.76}$	0.17 ± 0.02	12.02 ± 0.51	0.29 ± 0.05	2.89 ± 1.48	$1.18 \text{ pm } 0.72$	132.56 ± 6.93
$22.77^{+0.83}_{-0.81}$	0.12 ± 0.01	11.36 ± 0.43	-	1.92 ± 1.14	-	121.54 ± 7.12
$20.57^{+0.89}_{-0.87}$	0.07 ± 0.01	9.27 ± 0.41	-	-	-	106.07 ± 5.81
$18.14^{+0.97}_{-0.94}$	0.03 ± 0.01	5.65 ± 0.26	-	1.46 ± 0.95	-	95.92 ± 7.14
$15.43^{+1.08}_{-1.04}$	-	1.53 ± 0.12	-	-	-	123.79 ± 6.62
$12.34^{+1.27}_{-1.20}$	-	-	-	-	-	156.65 ± 8.20
$8.68^{+1.62}_{-1.43}$	-	-	-	-	-	209.38 ± 11.27
$3.94^{+2.25}_{-2.22}$	-	-	-	-	-	73.54 ± 5.70

Bibliography